

Numerical results for snaking of patterns over patterns in some 2D Selkov–Schnakenberg Reaction–Diffusion systems

Hannes Uecker, Daniel Wetzel

Institut für Mathematik, Universität Oldenburg, D26111 Oldenburg
hannes.uecker@uni-oldenburg.de daniel.wetzel@uni-oldenburg.de

November 7, 2018

Abstract

For a Selkov–Schnakenberg model as a prototype reaction-diffusion system on two dimensional domains we use the continuation and bifurcation software `pde2path` to numerically calculate branches of patterns embedded in patterns, for instance hexagons embedded in stripes and vice versa, with a planar interface between the two patterns. We use the Ginzburg-Landau reduction to approximate the locations of these branches by Maxwell points for the associated Ginzburg–Landau system. For our basic model, some but not all of these branches show a snaking behaviour in parameter space, over the given computational domains. The (numerical) non-snaking behaviour appears to be related to too narrow bistable ranges with rather small Ginzburg-Landau energy differences. This claim is illustrated by a suitable generalized model. Besides the localized patterns with planar interfaces we also give a number of examples of fully localized patterns over patterns, for instance hexagon patches embedded in radial stripes, and fully localized hexagon patches over straight stripes.

Keywords: Turing patterns, pinning, snaking, Ginzburg–Landau approximation, Maxwell point
MSC: 35J60, 35B32, 35B36, 65N30

Contents

1	Introduction	2
2	Numerical Results	6
2.1	Stripes, hexagons, and beans	6
2.2	Planar fronts, localized patterns and snaking in the hot bistable range	8
2.3	Time integration	11
2.4	Planar fronts, localized patterns and pinning in the cold range	12
2.5	Sideband patterns	15
3	Ginzburg-Landau reduction	16
3.1	Landau description of hexagons, stripes, and mixed modes	17
3.2	Ginzburg–Landau formalism and fronts	19
3.3	A modification with cold snakes and 1D snaking	22
3.4	1D snaking	23
4	Outlook: additional numerical results	25
4.1	Fully localized spot patches over radial stripes	25
4.2	An interface perpendicular to stripes	27
4.3	Fully localized (sideband) hexagon patches over straight stripes	27

arXiv:1304.1723v3 [math.DS] 15 Oct 2013

1 Introduction

Homoclinic snaking refers to the back and forth oscillation in parameter space of a branch of stationary localized patterns for some pattern forming partial differential equation (PDE). Two standard models are the quadratic–cubic Swift–Hohenberg equation (SHe)

$$\partial_t u = -(1 + \Delta)^2 u + \lambda u + \nu u^2 - u^3, \quad u = u(t, x) \in \mathbb{R}, \quad x \in \Omega \subset \mathbb{R}^d, \quad (1)$$

and the cubic–quintic SHe

$$\partial_t u = -(1 + \Delta)^2 u + \lambda u + \nu u^3 - u^5, \quad u = u(t, x) \in \mathbb{R}, \quad x \in \Omega \subset \mathbb{R}^d, \quad (2)$$

with suitable boundary conditions if $\Omega \neq \mathbb{R}^d$, and where $\lambda \in \mathbb{R}$ is the linear instability parameter, and $\nu > 0$.

In both equations the trivial solution $u \equiv 0$ is stable for $\lambda < \lambda_c := 0$, where in the 1D case $d = 1$ we have a pitchfork bifurcation of periodic solutions with period near 2π (“stripes”, by trivial extension to 2D, also called “rolls” due to their connection to Rayleigh–Bénard convection rolls). For $\nu > \nu_0 \geq 0$, with $\nu_0 = \sqrt{27/38}$ for (1) and $\nu_0 = 0$ for (2), the bifurcation is subcritical and the periodic branch starts with unstable small solutions r_- and turns around in a fold at $\lambda = \lambda_0(\nu) < 0$ to yield $\mathcal{O}(1)$ amplitude stable periodic solutions r_+ . Thus, for $\lambda_0 < \lambda < \lambda_c$ there is a bistable regime of the trivial solution and $\mathcal{O}(1)$ amplitude stripes.

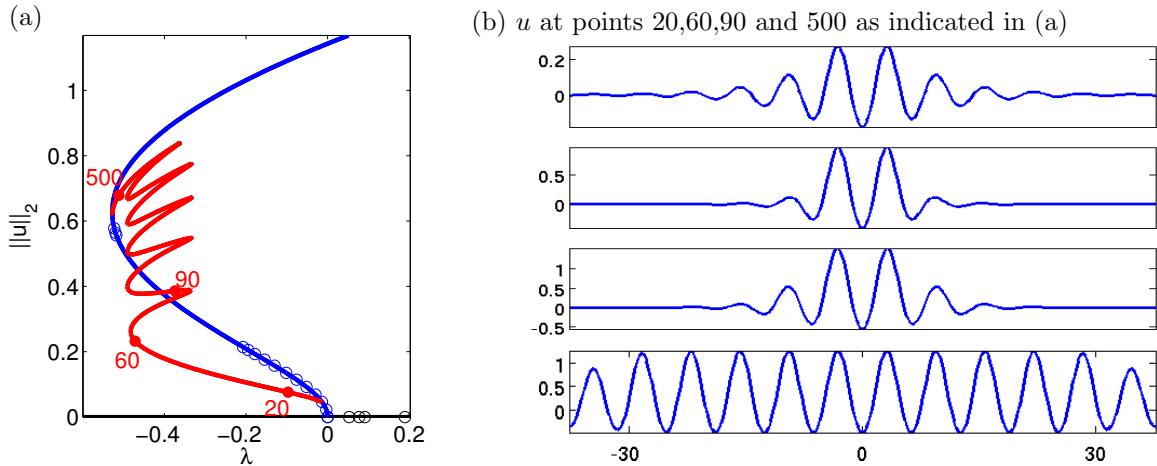


Figure 1: Illustration of homoclinic snaking in (1) over a 1D domain $x \in (-12\pi, 12\pi)$ with Neumann type boundary conditions $\partial_x u|_{x=\pm 12\pi} = \partial_x^3 u|_{x=\pm 12\pi} = 0$, $\nu = 2$. Here $\|u\|_2 := \left(\frac{1}{|\Omega|} \int_{\Omega} |u(x, y)|^2 dx dy \right)^{1/2}$. The branch r of primary roll solutions (blue) bifurcates subcritically at $\lambda = 0$ and becomes stable at $\lambda \approx -0.53$. Bifurcation points on the trivial branch and the roll branch are indicated by \circ , but omitted on the homoclinic snaking branch (red), which bifurcates from the second bifurcation point on r and reconnects to r just below the fold.

In the simplest case the localized patterns then consist of 1D stripes over the homogeneous background $u = 0$, and in each pair of turns in the snake the localized pattern grows by adding a stripe on both sides, and this continues for ever over the infinite line. See, e.g., [BK06, BK07, BKL⁺09] for seminal results in this setting, and [CK09, DMCK11] for detailed analysis using a Ginzburg–Landau formalism and beyond all order asymptotics. In finite domains snaking cannot continue for ever, and instead branches typically connect primary stripe branches, with either the same wave number or wave numbers near each other, see, e.g., [HK09, BBKM08, Daw09, KAC09] for detailed results, and Fig. 1 for illustration.

In 2D, by rotational invariance, depending on the domain and boundary conditions multiple patterns may bifurcate from $u \equiv 0$ at $\lambda = 0$, for instance straight stripes and so called hexagons. There are a number of studies of localized patterns for (1) and (2) over two dimensional domains [LSAC08, ALB⁺10], often combining analysis and numerics, and in more complicated systems like fluid convection [LJBK11]. See also [LO13] for recent results on snaking of localized hexagon patches in a 2-component reaction–diffusion system in 2D. However, all these works essentially consider patterns over a homogeneous background. Already in [Pom86] it is pointed out that “pinned” fronts connecting stripes and hexagons may exist in reaction-diffusion systems as a codimension 0 phenomenon in parameter space, i.e., for a whole interval of parameters. Similar ideas were also put forward in [MNT90] with the 2D quadratic–cubic SHe (2) as an example, see in particular [MNT90, Appendix C]. Such a pinned front is observed in [HMBD95] for (2) by time integration, but so far no studies of branches of stationary solutions involving different 2D patterns seem available.

Here we start with a standard model problem for predator (u) prey (v) reaction diffusion systems, namely

$$\partial_t U = D\Delta U + N(U, \lambda), \quad N(U, \lambda) = \begin{pmatrix} -u + u^2v \\ \lambda - u^2v \end{pmatrix}, \quad (3)$$

with $U = (u, v)(t, x, y) \in \mathbb{R}^2$, diffusion matrix $D = \begin{pmatrix} 1 & 0 \\ 0 & d \end{pmatrix}$, d fixed to $d = 60$, and bifurcation parameter $\lambda \in \mathbb{R}_+$. The reaction term N of (3) is a special version of $N(U, \lambda) = \begin{pmatrix} -u + u^2v + b + av \\ \lambda - u^2v - av \end{pmatrix}$, known as the Selkov [Sel68] ($a \geq 0, b = 0$) and Schnakenberg [Sch79] ($a = 0, b \geq 0$) model. For simplicity, here we set $a = b = 0$.

In particular we consider the stationary system

$$D\Delta U + N(U, \lambda) = 0. \quad (4)$$

The unique spatially homogeneous solution of (4) is $w^* = (\lambda, 1/\lambda)$. We write (4) in the form

$$\partial_t w = L(\Delta)w + G(w), \quad (5)$$

with $w = U - w^*$ and $L(\Delta, \lambda) = J(\lambda) + D\Delta$, where J is the Jacobian of N in w^* . For $\mathbf{k} = (m, n) \in \mathbb{R}^2$ we have $L(\Delta, \lambda)e^{i(mx+ny)} = \hat{L}(\mathbf{k}, \lambda)e^{i(mx+ny)}$, where $\hat{L}(\mathbf{k}, \lambda) = J(\lambda) - Dk^2$, $k := \sqrt{m^2 + n^2}$, and thus we also write $\hat{L}(k, \lambda)$. The eigenvalues of \hat{L} are given by $\mu_{\pm}(\mathbf{k}, \lambda) = \mu_{\pm}(k, \lambda) = \frac{\text{tr}\hat{L}(k, \lambda)}{2} \pm \sqrt{\left(\frac{\text{tr}\hat{L}(k, \lambda)}{2}\right)^2 - \det\hat{L}(k, \lambda)}$. Following [Mur89, Chapter 14] we find that in $\lambda_c = \sqrt{d}\sqrt{3 - \sqrt{8}} \approx 3.2085$ we have $\mu_+(\mathbf{k}, \lambda_c) = 0$ for all vectors $\mathbf{k} \in \mathbb{R}^2$ of length $k_c = \sqrt{\sqrt{2} - 1} \approx 0.6436$, and all other $\mu_{\pm}(\mathbf{k}, \lambda_c) < 0$, i.e., there is a Turing bifurcation at λ_c , with critical wave vectors $\mathbf{k} \in \mathbb{R}^2$ in the circle $|\mathbf{k}| = k_c$. The most prominent Turing patterns near bifurcation are stripes and hexagons, which modulo rotational invariance can be expanded as

$$\begin{aligned} U &= w^* + 2 \left(A \cos(k_c x) + B \cos\left(\frac{k_c}{2}(-x + \sqrt{3}y)\right) + B \cos\left(\frac{k_c}{2}(-x - \sqrt{3}y)\right) \right) \Phi + \text{h.o.t.} \\ &= w^* + 2 \left(A \cos(k_c x) + 2B \cos\left(\frac{k_c}{2}x\right) \cos\left(\frac{k_c}{2}\sqrt{3}y\right) \right) \Phi + \text{h.o.t.}, \end{aligned} \quad (6)$$

where $\Phi \in \mathbb{R}^2$ is the critical eigenvector of $\hat{L}(k_c, \lambda_c)$, and h.o.t. stands for higher order terms. The amplitudes $2A, 2B \in \mathbb{R}$ (where the factor 2 has been introduced for consistency with §3) of the corresponding Turing pattern depend on λ , with $A = B = 0$ at bifurcation. The stripes bifurcate in a supercritical pitchfork, the hexagons bifurcate transcritically, and the subcritical part of the hexagons is usually called “cold” branch as here u has a minimum in the center of each hexagon.

In §2 and §4 we present some numerically calculated Turing patterns for (4), including so called mixed modes, and, moreover, some branches of stationary solutions which involve different patterns, namely

- (a) planar fronts between stripes and hexagons, and associated localized patterns, e.g., hexagons localized in one direction on a background of stripes (see Fig.2(a),(b) for an example), and vice versa;
- (b) fully 2D localized patches of hexagons over a homogeneous background, and over radial and straight stripes (see Fig.2(c),(d),(e) for examples).

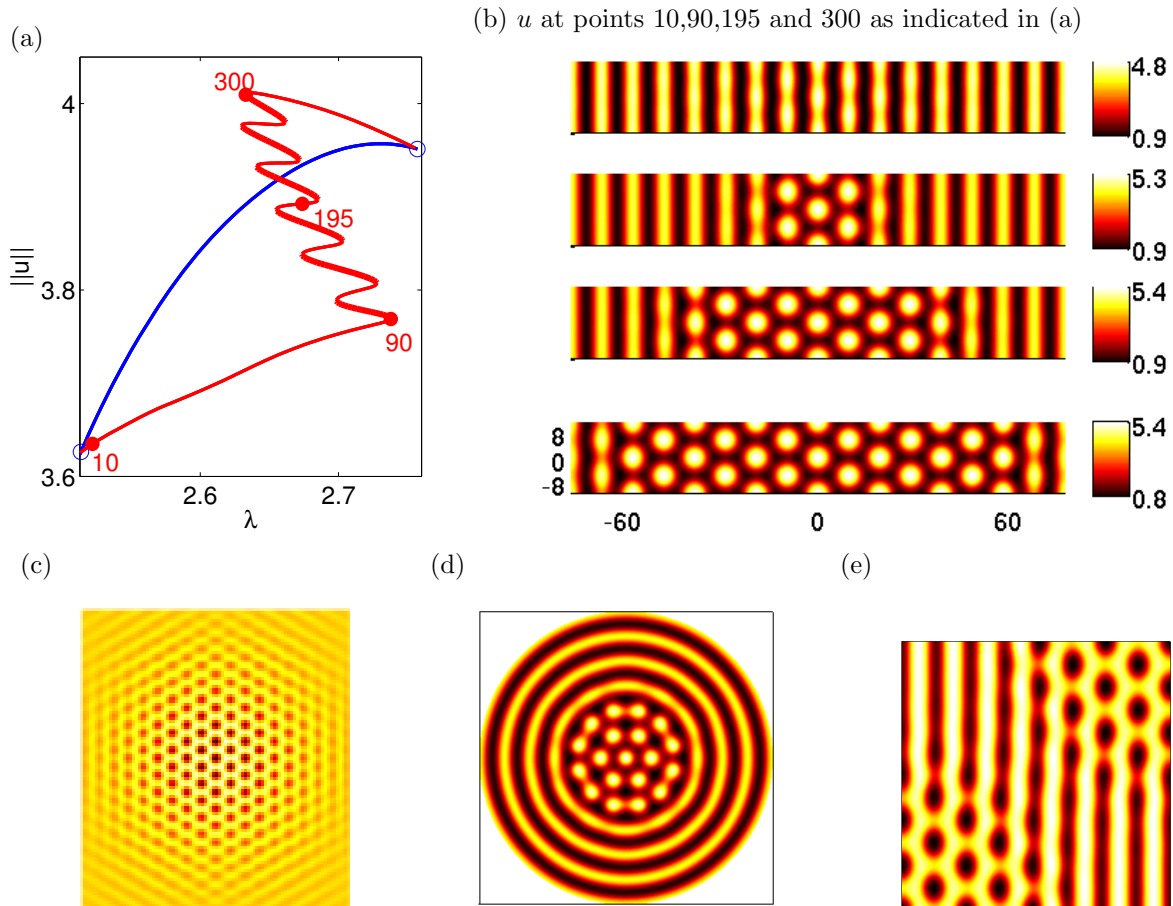


Figure 2: (a), (b) Mixed mode branch (blue) in the RD system (4) which connects stripes and hexagons, and a branch of hexagons on a background of stripes. Here $\|u\| = \|u\|_{L^8} := \left(\frac{1}{|\Omega|} \int_{\Omega} |u(x,y)|^8 dx dy \right)^{1/8}$ was chosen for purely graphical reasons. (In Fig. 1 any L^p norm can be used to illustrate the snaking, but for (4) the stripes and hexagons have rather similar L^2 norms.) This example will be discussed in much more detail below, and here we mainly want to point out the similarities with Fig. 1. In Fig. 1 the snaking branch is in the bistable range of (large) amplitude rolls and the homogeneous background, here it is in the bistable range of stripes and hexagons. In both cases the snaking branch bifurcates from an unstable branch connecting two different stable branches, and after bifurcation first needs a long transverse to enter the “snaking region”. Finally, in both cases, the snaking branches consist of stable solutions after every second fold, indicated here by thicker lines.

(c)-(e) u for fully localized spot patterns over homogeneous background (c), and over radial (d) and straight (e) stripes. See below for colorbars and spatial scales. (d) and (e) again lie on some snaking branches, see §4.1 and §4.3, while the branch for (c) numerically does not snake, see §2.4. However, a snaking branch of patterns as in (c) can be obtained for the modified system (7) below, see §3.3.

Related to the transcritical bifurcation of the hexagons, the patterns in (a) come in two regimes: one “hot” which is rather far from the primary bifurcation at λ_c ; one “cold”, with λ closer to λ_c . Of these, only the “hot” branches show snaking behaviour in our numerical simulations for (4).

For (1) and (2) it is known (e.g., [KC06], [DMCK11]), that the “snaking width” is exponentially small in the properly defined subcriticality parameter ε . We expect a similar result here, which explains why snaking in the cold regimes might be below the numerical resolution. To make this quantitative we modify (3) to make the system “more subcritical” in the cold regime, and in this way we can switch on cold snaking, i.e., find it numerically.

First, however, in §3 we relate our numerical results to arguments derived from the Ginzburg–Landau reduction. One result is the calculation of Ginzburg–Landau Maxwell points, which give predictions for the λ –ranges of the fronts and localized patterns in the full system (4). In fact, for a consistent Ginzburg–Landau reduction of (3) in principle one should include the parameters a, b from $N(U, \lambda) = \begin{pmatrix} -u + u^2v + b + av \\ \lambda - u^2v - av \end{pmatrix}$, to locate a co–dimension 2 point where the quadratic terms in (5) scale suitably. However, then the algebra for the bifurcation analysis will become even more involved. Moreover, here we are explicitly interested in phenomena $\mathcal{O}(1)$ away from $(w, \lambda) = (0, \lambda_c)$, and thus rather explore how far the Ginzburg–Landau reduction can take us.

Then, motivated by the Ginzburg–Landau reduction, we modify the system (3) to

$$\partial_t U = D\Delta U + N(u, \lambda) + \sigma \left(u - \frac{1}{v} \right)^2 \begin{pmatrix} 1 \\ -1 \end{pmatrix}. \quad (7)$$

We do not claim any biological meaning for the term multiplied by σ , but the advantage of this modification is that the homogeneous solution and the linearization around it are unchanged, the Turing bifurcation is still at λ_c , and only the nonlinear terms in (5) are affected. Our first goal is to increase the subcriticality of the cold hexagons to obtain homoclinic snaking for branches connecting these with $w = 0$. Similarly, via σ we can increase the bistability range between cold stripes and cold hexagons and thus we can also switch on snaking in this regime. Finally, while (4) has no bistability between stripes and $w = 0$ and thus no homoclinic snaking in 1D can be expected, in (7) we can also turn the bifurcation of stripes from supercritical to subcritical to obtain 1D homoclinic snaking between stripes and $w = 0$, see §3.4.

Section 4 contains additional numerical results about fully localized patterns over patterns, namely (hexagonal) spots over radial stripes, and fully localized (hexagonal) spots over straight stripes, respectively, see also Fig. 2(d),(e). The numerics for such patterns are quite demanding, and therefore we restrict to some illustrative examples.

Thus, the remainder of this paper is organized in a slightly unconventional way, which is partly due to our own “experimental mathematics” approach, as newcomers to the field of homoclinic snaking: First we numerically calculated the Turing bifurcation diagram and spotted the hot snaking branches and the non-snaking cold localized branches, then we started the Ginzburg–Landau reduction to *a posteriori* get some analytical understanding, mainly via Maxwell points. Then, however, we used the Ginzburg–Landau reduction as a *predictive tool* to find ranges for the modified systems where we could switch on the cold snaking, and the 1D snaking via subcritical bifurcations of stripes. We believe that it is more honest to also present our results in that order, instead of trying to first present as much theory as possible and then use numerics only for illustration. More importantly, we believe that this makes the paper also more readable.

In §5 we give with a brief discussion. We believe that the results are not specific to the model system (4) but can be expected in any reaction diffusion system (over sufficiently large domains) with a bistability between different patterns which allow homo–or heteroclinic connections in the associated Ginzburg–Landau system. Finally, we close with a short list of Open Problems.

Acknowledgements. We thank Jonathan Dawes for helpful discussions, and two anonymous referees for a critical reading of the first version of this manuscript and many helpful questions and remarks, which in particular motivated us to set up the modified system (7), and some of the numerics in §4.

2 Numerical Results

2.1 Stripes, hexagons, and beans

We use the bifurcation and continuation software `pde2path` [UWR13] to numerically calculate patterns for (4), and their stability. We start with domains of type $\Omega = (-l_x, l_x) \times (-l_y, l_y)$, $l_x = 2l_1\pi/k_c$, $l_y = 2l_2\pi/(\sqrt{3}k_c)$, $l_1, l_2 \in \mathbb{N}$, with Neumann boundary conditions, chosen to accommodate the basic stripe and hexagon patterns.¹

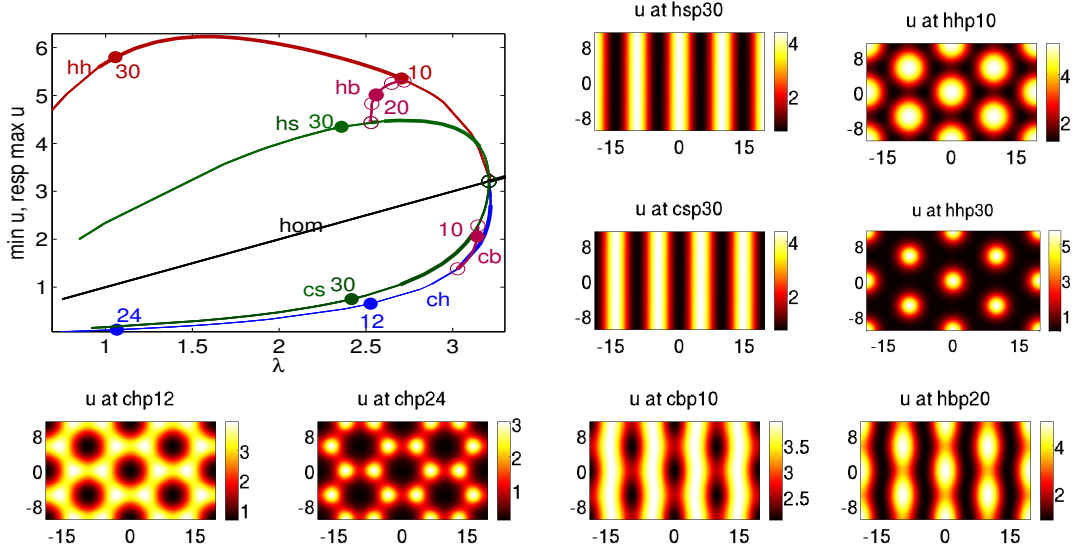


Figure 3: Bifurcation diagram and example solutions of (4) obtained with `pde2path` over the “ 2×2 ”-domain $\Omega = (-l_x, l_x) \times (-l_y, l_y)$ with Neumann boundary conditions, $l_x = 4\pi/k_c$, $l_y = 4\pi/(\sqrt{3}k_c)$, $k_c = \sqrt{\sqrt{2}-1} \approx 0.6436$. The branch `hom` are the homogeneous solutions, `hs` the hot (up) stripes, `cs` the cold (down) stripes, `hh` the hot hexagons, and `ch` the cold hexagons. For instance `hsp30` stands for the 30th point on the branch `hs`. `hb` and `cb` are mixed mode branches, which we call hot and cold beans, respectively. For `hs`, `hh`, and `hb` we plot the maximum of u , and the minimum for `cs`, `ch`, and `cb`. Stable and unstable parts of branches are represented by thick and thin lines, respectively. In particular, except for `hhp10`, `hhp30` all displayed patterns are unstable. Only a small selection of bifurcation points is indicated by \circ . See [UW13] for a movie.

In Fig. 3 we use the rather small $l_1 = l_2 = 2$, which we call a 2×2 domain as in both directions 2 hexagons “fit”. The main panel shows a part of the very rich bifurcation diagram. Following biological terminology we classify the stripes ($A \neq 0$, $B = 0$ in (6)) into hot (also called “up”) stripes (`hs`, $A > 0$) and cold (also called “down”) stripes (`cs`, $A < 0$), which exhibit a maximum respectively a minimum at $x = 0$. We always plot u . If we have a hot pattern for u , then v is a cold pattern and vice versa. This follows from the predator-prey structure of the reaction term N of (4). The stripes are $2\pi/k_c$ -periodic in the horizontal direction, bifurcate in a supercritical pitchfork, and are stable from $\lambda_s^b \approx 3.15$ to $\lambda_s^e \approx 2.51$, where here and henceforth the subscript of the bifurcation parameter λ denotes the branch and the superscript stands for ending or beginning of stability. The hexagons ($A = B \neq 0$) can be classified into hot hexagons (`hh`, $A = B > 0$) and cold hexagons (`ch`, $A = B < 0$), which have a maximum resp. a minimum in the center of every hexagon. They are $4\pi/k_c$ -periodic in the horizontal and $4\pi/(\sqrt{3}k_c)$ -periodic in the vertical direction. The hexagon branch bifurcates transcritically from the homogeneous branch at $\lambda = \lambda_c$.

¹In [UWR13, §4.2] we set $l_y = 2\delta l_2\pi/(\sqrt{3}k_c)$, where the slight “detuning” $\delta \approx 1$ is used to unfold the multiple bifurcation at $\lambda = \lambda_c$ since `pde2path` currently only deals with simple bifurcations. However, by carefully choosing λ stepsizes for λ near λ_c the discretization error is enough to do this unfolding and thus we drop δ here, i.e., set $\delta = 1$. The bifurcation diagram and solution plots for $\delta = 1$ and $\delta = 0.99$ are visually indistinguishable.

It “starts” in a saddle node or fold bifurcation at $\lambda_{ch}^b \approx 3.22$, and the stability region of the cold hexagons begins at the fold and ends in $\lambda_{ch}^e \approx 3.03$. The hot hexagons are stable from $\lambda_{hh}^b \approx 2.73$ to $\lambda_{hh}^e \approx 0.98$.

Thus, there is a bistable range of cold stripes and cold hexagons for $\lambda \in (\lambda_{ch}^e, \lambda_s^b)$, of hot stripes and hot hexagons for $\lambda \in (\lambda_s^e, \lambda_{hh}^b)$, and of cold hexagons and the homogeneous solution for $\lambda \in (\lambda_c, \lambda_{ch}^b)$. A branch of “skewed hexagon” or “mixed mode” solutions of the form (6) with $A < B < 0$ bifurcates subcritically from the cold hexagon branch **ch** in λ_{ch}^e and terminates on the cold stripe branch **cs** in λ_s^b . Following [Yan04] we call this type of solutions cold *beans* (**cb**). There is also a branch **hb** of hot beans with $A > B > 0$ which bifurcates subcritically from the hot stripe branch **hs** in λ_s^e and terminates on the hot hexagon branch **hh** in λ_{hh}^b .

Remark 2.1. For all these patterns the discrete symmetry $\mathcal{S} = S_{2\pi/k_c}$ given by the shift by $2\pi/k_c$ in the horizontal direction yields a solution as well. The stripes are of course invariant under \mathcal{S} , but for the hexagons the shifts generate new branches **S**hh and **S**ch. These make the plotting of the bifurcation diagram a bit complicated graphically. Therefore, in Fig. 4 we repeat the bifurcation diagram from Fig. 3 in a schematic way, with ordinate $u(0,0)$, i.e., u in the center of the domain, and add the branches of shifted hexagons. The bean branches **hb** and **cb** then both take part in a “loop” involving shifted beans and so called rectangles, which again can be expanded as in (6), now with $|A| \leq |B|$, but which are generically unstable. This can be worked out on the level of amplitude equations, see §3, and it is also recovered by our numerics for the full system. The behaviour described below like snaking branches bifurcating from hot beans obviously transfers to branches related by \mathcal{S} . In the following we mainly focus on the **hb** and **cb** branches, and also mostly restrict to following just one direction at bifurcation.]

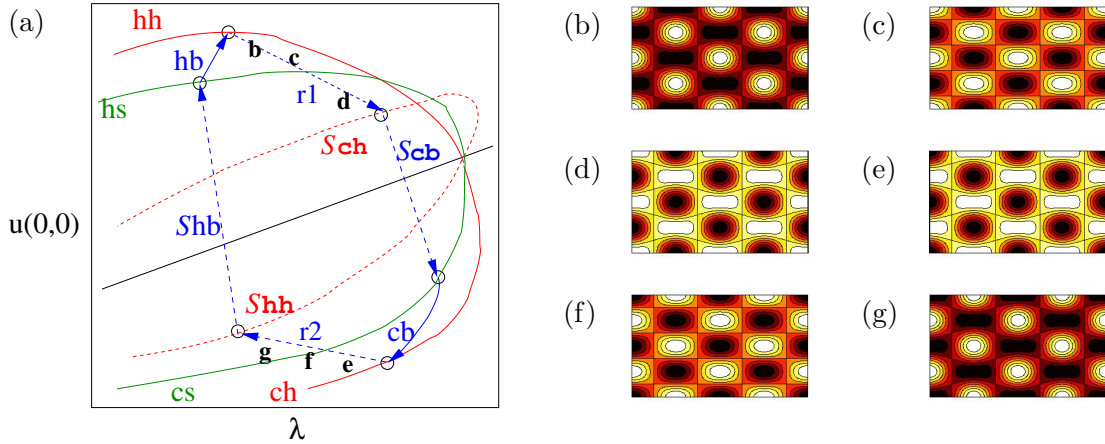


Figure 4: (a) Schematic bifurcation diagram with $u(0,0)$ as ordinate. Additional branches compared to Fig. 3 are dashed, and **S*** denotes the respective phase shifted pattern, i.e., **S**hh are the phase shifted hot hexagons. **hb** and **cb** both form part of a loop $hs \xrightarrow{hb} hh \xrightarrow{r1} S^*ch \xrightarrow{S^*cb} cs \xrightarrow{cb} ch \xrightarrow{r2} S^*hh \xrightarrow{S^*hb} hs$, where **r1** and **r2** are called rectangles. (b)–(d) **r1** example solutions for which, in the expansion (6), $B > 0$ and A changing from $A > 0$ in (b) via $A = 0$ in (c) to $A < 0$ in (d). (e)–(f) **r2** with $B < 0$ and A changing from $A < 0$ in (e) via $A = 0$ in (f) to $A > 0$ in (g). (b)–(d) correspond to “hot” solutions with a maximum in the middle of the domain and hence in the middle of the central hexagon, while (e)–(g) illustrate “cold” solutions with a minimum in the middle of the domain.

Remark 2.2. The main regime of interest to us is $\lambda \in [2.5, 3.22]$, and below $\lambda \approx 2.5$ all branches plotted except **hh** are unstable. We plot a somewhat larger bifurcation picture since, e.g., on the **ch** branch some interesting patterns occur.]

Remark 2.3. (a) `pde2path` uses the Matlab FEM `pdetoolbox` to discretize elliptic PDEs like (4), including some error estimators and adaptive mesh-refinement, see [UWR13] for details. In Fig. 3

we used a regular “base mesh” of 20.000 triangles which, e.g., on the beans branch is refined to about 60.000 triangles on average. Moreover, for all solutions calculated the mesh can be further refined to yield arbitrary small error estimates without visible changes to the solutions. Calculation time for the full bifurcation diagram in Fig. 3 on a quad core desktop PC is about 40 Minutes. The `pde2path` script to generate Fig. 3 is also included in the software as demo `schnakenberg`, and a movie running through the bifurcation diagram of Fig. 3 and some more movies are collected at www.staff.uni-oldenburg.de/hannes.uecker/pde2path/schnakmov.html.

(b) The rather large numbers of triangles was needed mainly in order to avoid uncontrolled branch switching, and it is the large number of different branches which makes the continuation and bifurcation numerics of (4) demanding. For instance, on the 2×2 domain the first 10 bifurcations from the homogeneous branch occur between $\lambda = \lambda_c \approx 3.2085$ and $\lambda_{10} \approx 3.1651$. On larger domains, these bifurcation points collapse to λ_c . For instance, over the 6×2 domain used in Fig. 10 below we have $\lambda_{10} \approx 3.2042$. Similarly, on all branches shown in Fig. 3 there are many bifurcation points, and thus we only plot a small part of the bifurcation diagram. See [UWR13] on details how `pde2path` tries to avoid branch jumping.

(c) The branches plotted in Fig. 3 stay the same over all $l_1 \times l_2$ domains with $l_1, l_2 \in \mathbb{N}$, $l_1, l_2 \geq 2$. However, stability of solutions of course may change. For instance, taking a larger l_2 , the hot stripes no longer loose stability at bifurcation of the *regular* beans, i.e., with fundamental wave-vectors $k_1 = k_c(1, 0)$, $k_{2,3} = k_c(-\frac{1}{2}, \pm\frac{\sqrt{3}}{2})$ forming an equilateral triangle. Instead, *stretched* beans with sideband wave vectors $\tilde{k}_{2,3} \approx k_{2,3}$, $\tilde{k}_{2,3} \neq k_{2,3}$, bifurcate more early, i.e., for larger λ . See, e.g., §4.3. In the following we first keep $l_2 = 2$ fixed and consider larger l_1 , which will give interfaces between stripes and hexagons parallel to the (vertical) stripes. In §4 we look at some other interface angles between, e.g., hexagons and stripes. This, however remains only an outlook on the complicated problem of interface orientation.

(d) To use `pde2path` for 1D problems like in Fig. 1, see also §3.4, we artificially set up a thin strip and use Neumann boundary conditions in transverse (here y) direction such that solutions are constant in y , e.g., $\Omega = (-12\pi, 12\pi) \times (l_y, l_y)$ with small $l_y = 0.1$ in Fig. 1. To keep computations cheap but accurate, l_y and the initial mesh are chosen in such a way that we have only two grid points in y direction, and that the triangles are roughly equilateral. The number of “grid points in y -direction” may then change under mesh-refinement, but the mesh quality is controlled automatically.

(e) Finally, the current version of `pde2path` as such only detects and deals with simple bifurcations in the sense that a simple eigenvalue goes through zero. Thus, no Hopf bifurcations are detected. By counting the number of negative eigenvalues we can however check for Hopf bifurcations a posteriori, see §3.4 for an example.]

2.2 Planar fronts, localized patterns and snaking in the hot bistable range

To reduce computational costs, but also for graphical reasons, in Fig. 3 we used a rather small domain for the basic bifurcation diagram. We now present simulations on larger domains, where however we still restrict to intermediate sizes. Again, this is mainly due to graphical reasons, and we remark that all results can be reproduced on larger domains, at least qualitatively.

Counting from the `hs` branch, `pde2path` yields four bifurcation points `hbbp1`, `hbbp2`, `hbbp3` and `hbbp4` on the hot bean branch `hb`. One bifurcating branch connects `hbbp1` and `hbbp4`, and another branch connects `hbbp2` and `hbbp3`. By doubling the horizontal length to a 4×2 domain, i.e., setting $l_x = 8\pi/k_c$, we find eight bifurcation points `hbbp1`, ..., `hbbp8` on `hb`, see Fig. 5, where now as in Fig.2 we use

$$\|u\| = \|u\|_{L^8} := \left(\frac{1}{|\Omega|} \int_{\Omega} |u(x, y)|^8 d(x, y) \right)^{1/8} \quad (8)$$

as the main solution measure. This choice is quite arbitrary, but by trial and error we found it more suitable to display branches snaking between different patterns than the usual L^2 norm, which works well for snaking of patterns over some homogeneous background.

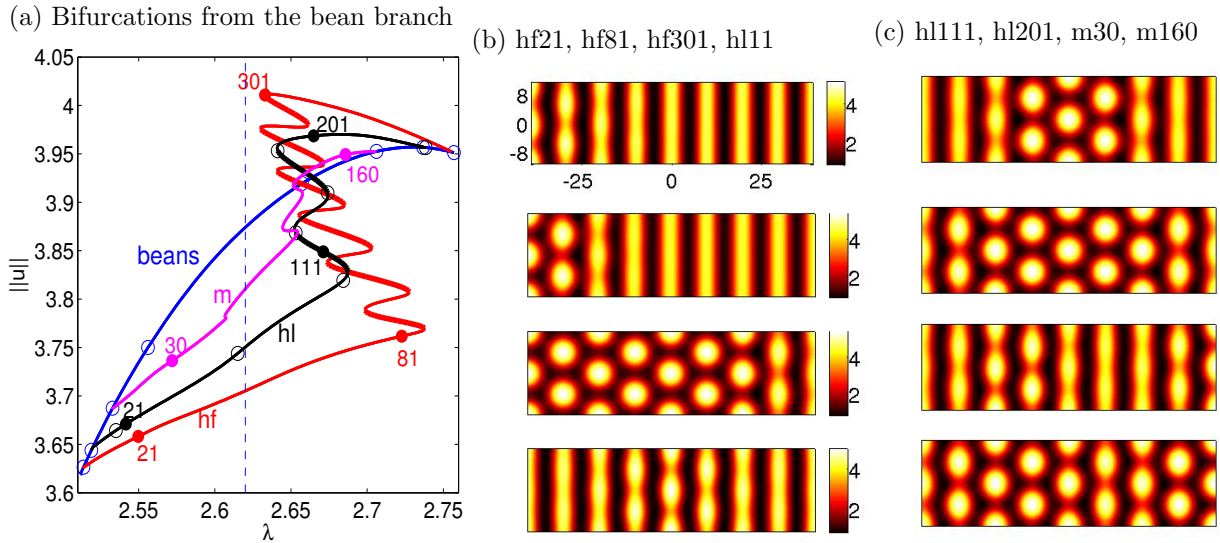


Figure 5: Bifurcation diagram and example plots of fronts and localized patterns of (4) obtained with `pde2path` over a 4×2 domain; $\lambda_m \approx 2.62$ is the so called (Ginzburg–Landau) Maxwell point, see §3. In (b), for instance `hf21` means the 21st point on the “hot front” branch in (a), and similar for `hl*` and `c*`. Domain in all plots as in the first plot in (b), and the colormap is roughly constant. Bifurcation points (in (a) only shown on the bean and the `hl` branches) are indicated by \circ , stable and unstable parts of branches by thick and thin lines, respectively. See [UW13] for a movie.

The branches bifurcating in `hbbp1` and `hbbp2` are called `hf` (hot front) and `hl` (hot localized), respectively. Some example solutions on `hf` and `hl` are also presented, and the so called Ginzburg–Landau Maxwell point λ_m . The `hf` branch connects `hbbp1` to `hbbp8`, and contains stationary fronts U_{het} from hot hexagons to hot stripes, while `hl` connects `hbbp2` to `hbbp7` and contains homoclinic solutions U_{hom} in the form of localized hexagons embedded in stripes. More precisely, the branches take part in closed loops, e.g., the `hf` branch is one half of a loop containing `hbbp1` and `hbbp8`, the other half containing hexagons coming into the domain from the right. Again we generally only discuss parts of each of these closed loops.

Both branches, `hf` and `hl`, show a snaking behaviour in the bifurcation diagram, and we first discuss the `hl` branch which indicates the start of so called homoclinic snaking, which becomes more prominent if we further increase the domain size, cf. Fig.2. On `hl`, looking from `hbbp2` to `hbbp7`, during each cycle consisting of two folds, a further hexagon is added on both sides of the hexagon patch localized in the middle over a background of stripes. The parts of the snake pointing north–west contain stable solutions, while on the parts pointing north–east there are 2 unstable eigenvalues. The transitions from unstable to stable parts thus proceed via the folds and additional bifurcation points, discussed below.

In contrast to theory and also to 1D problems over very large domains, the branch does not snake around a vertical line but in a slanted manner. This, and the fact that the branch does not directly bifurcate from the stripes but from the beans, are finite size effects, cf. [BCR08, BBKM08, HK09, Daw09]. During, e.g., the initial traverse from `hbbp2` to the third bifurcation point the “near stripe bean pattern” at the bifurcation point is reshaped to hexagons in the middle and stripes at the sides. The analogous reshaping to “near hexagon beans” takes place between `hlp201` and `hbbp7`.

In 1D models like (1) and (2), in theory, and over sufficiently large domains with periodic

boundary conditions, bifurcation points near the folds of a homoclinic snake are usually associated with “rungs” which together with a snake of the same wave number patterns but different parity (i.e., odd instead of even) form ladders, see in particular [BKL⁺09]. In our case, due to the Neumann boundary conditions there is no snake of odd solutions with wave number k_c (see however §2.5 for “odd sideband snakes”). Thus, it is interesting to see the behaviour of branches bifurcating from the bifurcation points near the folds, which we illustrate in Fig. 6. These points are again pairwise connected. On, e.g., the first horizontal part of the q branch the solutions try to develop an odd symmetry around $x = \pi/k_c$ by growing/decreasing hexagons on the right/left. However, this cannot connect to the missing odd snake, and the branch turns around to a diagonal segment which would belong to the odd snake. Thus, this behaviour is again very much a finite size and boundary conditions effect, and similar comments apply to the r branch.

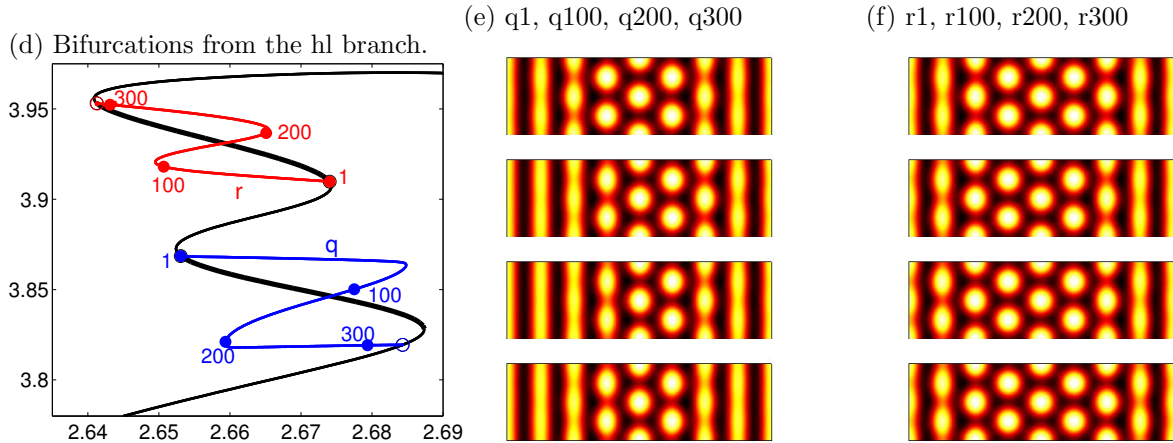


Figure 6: A magnification of the hl branch from Fig. 5, and the “rung type” branches connecting bifurcation points on the hl branch, and some show example plots. The diagonal parts of the q and r branches can be seen as fragments of a $\pi/k_c c$ shifted odd snake with wave number k_c , which does not exist over the given domain with homogeneous Neumann boundary conditions. See text for details, and [UW13] for a movie.

Remark 2.4. For both, the 1D cubic quintic SHe (2) and the quadratic cubic SHe (1), an analogon of the bean branch is the branch r_- of small amplitude unstable stripes that bifurcates subcritically from $(u, \lambda) = (0, 0)$ and “connects” to the fold where the stripes become stable, cf. Fig. 1. In [Daw09] the appearance of bifurcation points on r_- is related to modulational instability of the amplitudes $A_-(\lambda)$ of the unstable stripes in the associated Ginzburg–Landau equation, derived by using a scaling of the “subcriticality parameter” ν in (2). In particular, this gives a lower bound on the domain size necessary for these bifurcations, which is linear in $1/\nu$, i.e., inversely proportional to the subcriticality. Moreover, it explains why the bifurcations occur in connected pairs like (in our case) $(hbbp1, hbbp8)$, $(hbbp2, hbbp7)$, and so on. Similarly, using beyond all order matched asymptotic expansions, a number interesting results for finite size effects on the snaking branches in the 1D quadratic cubic SHe are obtained in [KAC09], including that larger domains yield smaller pinning ranges, i.e., more narrow snakes.

At least the relation between subcriticality of the equation and necessary domain size for secondary bifurcations also holds for our system, see Remark 2.5. We expect that calculations similar to those in [Daw09] and in [KAC09] can also be done in our case using the system of Ginzburg–Landau equations derived in §3 (and extensions as in [KAC09]), but naturally they will be more complicated.]

In contrast to the homoclinic snaking of the hl branch which at least for simpler models on infinite cylinders can be also explained and predicted theoretically, see §3, finite size effects should be regarded as essential for the “heteroclinic snaking” of the hot front branch hf in Fig. 5. In

fact, at least for the 1D Swift–Hohenberg equation, beyond all order asymptotics [CK09] predict that for each λ near the Maxwell point there are at most two pinned front solutions, again see §3. Thus, the hot fronts should be seen as homoclinics by even extension of the solutions over the left boundary (hexagons on a background of stripes) or right boundary (stripes on a background of hexagons). See also Fig. 7 below. The m (as in multiple) branch, consists of solutions with multiple fronts between stripes and hexagons.

To further assess the finite size effects, in Fig. 7 we plot homoclinic snakes from the second bifurcation points on the bean branches over 8×2 and 12×2 domains. The 8×2 branch (see also

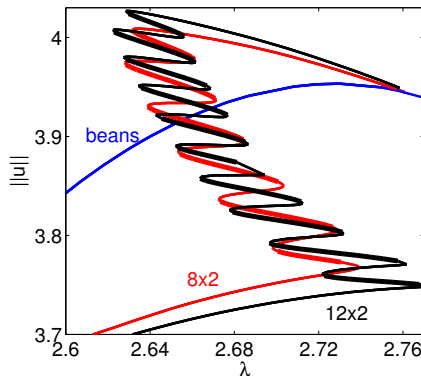


Figure 7: Hot homoclinic snaking over 8×2 and 12×2 domains.

Fig. 1) is very close to the hf branch of the 4×2 domain, thus justifying the claim that the 4×2 hf branch should be seen as a 8×2 $h1$ branch by mirroring it over the left boundary. Remarkably, the 12×2 $h1$ branch is *more* slanted than the 8×2 branch. This agrees with the trend already seen in Fig. 5 by comparing the 4×2 hf and $h1$ branches, and can be further confirmed by considering even larger domains, but is contrary to numerical and analytical results for 1D snaking, see in particular [KAC09] for the 1D quadratic cubic SHE (1). There, as the domain size increases, snaking becomes *more* confined around the Maxwell point of the variational equation (1) and less slanted. At this point we cannot offer an explanation for Fig. 7, but can only point out that our system is not variational. Therefore, Maxwell points and energy arguments can only be given approximately by asymptotic expansions, see §3, and the λ regime discussed so far is quite far from the primary bifurcation. Moreover, we also have to deal with a possibly rather complicated interaction between the length in x , which we increased, and the length in y , which we fixed, on the one hand to keep calculational costs at base, but also to first vary only one size parameter. In fact, below we shall find snakes which are much less slanted than those in Fig. 7. These are typically found much closer to λ_c , and moreover involve different ratios between x and y wavenumbers, see for instance Fig. 12.

2.3 Time integration

The stability information in Figures 3, 5, 6 and 7 is based on the spectrum of the linearization around a (FEM) solution. Given the rather large and complicated space of solutions it is interesting to assess the nonlinear stability and basin of attraction of solutions. For this we use time integration of the spatial FEM discretization of (4) by some standard semi implicit method. This is also quite useful to quickly obtain nontrivial starting points for continuation and bifurcation. Generally speaking, we obtain desired stable target solutions from only rough initial guesses, where typically we integrate for some rather short time and then use a Newton loop for the stationary problem to get to the stationary solution. See Fig. 8 for an example, where, with $A=0.3$, $B=0.15$ and $L=12$,

$$U_0 = \left(\begin{array}{c} \lambda \left(1 + A \cos(k_c x) + \operatorname{sech}\left(\frac{x}{L}\right) [2B \cos\left(\frac{k_c}{2} x\right) \cos\left(k_c \frac{\sqrt{3}}{2} y\right) - 0.1 \cos(k_c x)] \right) \\ \frac{1}{\lambda} \left(1 - \frac{1}{2} \left(A \cos(k_c x) + \operatorname{sech}\left(\frac{x}{L}\right) [2B \cos\left(\frac{k_c}{2} x\right) \cos\left(k_c \frac{\sqrt{3}}{2} y\right) - 0.1 \cos(k_c x)] \right) \right) \end{array} \right). \quad (9)$$

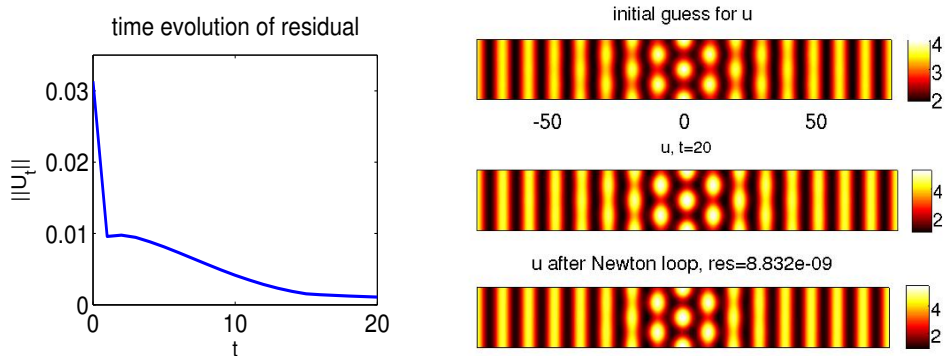


Figure 8: Finding a pattern from an initial guess and time integration, on an 8×2 domain. Here $\lambda=2.7$, U_0 from (9). For this U_0 , a Newton loop for the stationary problem does not converge, but it does after decreasing the residual $\|\partial_t U\|_\infty$ by a number of time steps, where U denotes the spatial discretization of U .

Although motivated by the desired mode structure, the precise form of (9) is rather arbitrary. We obtain convergence to “hot localized” solution, where of course the width of the hexagon patch over the stripe background, i.e., the position in the snake, depends on the initial width L .

Another interesting numerical experiment is to choose an initial point on a snaking branch and externally modifying λ to some other value. For instance, in Fig. 9 we use the stationary solution U for $\lambda = 2.7$ from Fig. 8 and modify λ to $\lambda = 2.65$, which is still inside the snaking region, and to $\lambda = 2.6$, which is just outside. To illustrate the time evolution of $u(t, x, y)$ we plot a space time diagram of $u(\cdot, \cdot, -l_y)$, i.e., of u on the lower boundary of Ω . In these the hexagons appear as “rolls” with double the wavelength of the stripes due to $|k_x| = \frac{1}{2}k_c$ for hexagons. For both, $\lambda = 2.65$ and $\lambda = 2.6$, we observe two fronts moving outwards with a “stick-slip” motion, where $n(t) := \|u(t, \cdot, \cdot)\|$ becomes flat as $u(t, \cdot)$ comes close to the (here left) folds in the 8×2 snaking branch from Fig. 7. For $\lambda = 2.6$ we then end up with space filling hexagons, and for $\lambda = 2.65$ with some localized hexagons “further up” on the snake, which again shows stability of these solutions.

(a) $\lambda=2.65$, conv. to localized hexagons further up the snake (b) $\lambda = 2.6$, conv. to space filling hexagons (c) Norm evolution

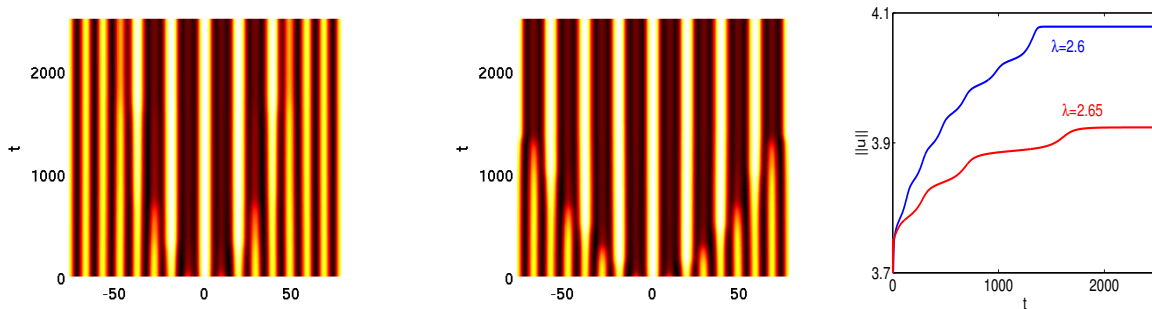


Figure 9: Stick-slip motion after “stepping out of the snake”; (a), (b) $u(t, x, -l_y)$ in space–time diagram, initial conditions from Fig. 8.

2.4 Planar fronts, localized patterns and pinning in the cold range

On the cold bean branch **cb** there are no bifurcation points over a 2×2 or 4×2 domain. However, Fig.10(a) shows 4 of the 8 bifurcation points obtained on the cold bean branch over a 12×2 domain, namely **cbbp1**, **cbbp2**, **cbbp7**, **cbbp8**, the branch **cf** (cold front) connecting **cbbp1** and **cbbp8**, and the branch **c1** connecting **cbbp2** and **cbbp7**, and consisting of hexagons on a stripe background.

Panel (b) shows 4 example solutions. In, e.g., c150 it can be seen that the localized hexagons are shifted by $2\pi/k_c$ in x , such that here we really consider \mathcal{S}_{cb} which connects cs to \mathcal{S}_{ch} , cf. Remark 2.1, but for simplicity we omit the \mathcal{S} .

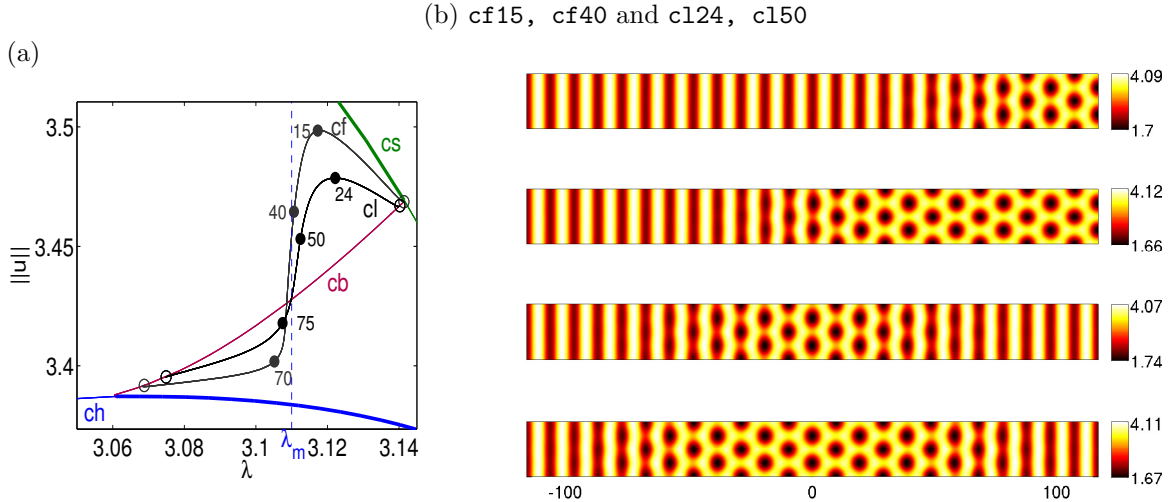


Figure 10: Bifurcation from the cold beans on a 12×2 domain. (a) cf branch connecting $cbbp1$ with $cbbp8$ in a monotonous way (no snaking), cold localized branch $c1$, and the cold Maxwell point (see §3). (b) Some example solutions. See [UW13] for a movie.

Similar to Fig. 5, after bifurcation from, e.g., $cbbp1$, in the traverse to $cf15$ the solutions reshape into stripes on the left and hexagons on the right. The growth of the hexagon part then happens in a narrow λ regime around λ_m between $cf15$ and $cf70$, while between $cf70$ and $cbbp8$ the solutions are reshaped to near hexagon beans. Similar remarks hold for the $c1$ branch.

The third bistable range we discuss is between the homogeneous solution $w^* = (\lambda, 1/\lambda)$ and the cold hexagons for $3.21 \approx \lambda_c < \lambda < \lambda_{ch}^b \approx 3.22$. Here, over sufficiently large domains, we have bifurcation points on the small amplitude (unstable) cold hexagon branch, which now corresponds to the r_- branch for (2) in Fig. 1. As above we can find quasi 1D fronts between w^* and cold hexagons, see Fig. 11(e), and the associated 1D localized patterns. However, as in the qcSHe (1) and the cqSHe (2), see [ALB⁺10] and the references therein, we can also calculate fully localized patches of hexagons, see Fig. 11(a)–(d).

Remark 2.5. An essential difference between Fig. 5 and Figures 10 and 11 is that in the latter there is no snaking. Starting with Fig. 10 and following Remark 2.4 we believe that the need for a large domain to obtain bifurcations from the cb branch can be explained from the “weak subcriticality” of the system in this range, such that the cold bistable range is rather narrow, compared to the hot bistable range. Related to this, the difference in (Ginzburg–Landau–)energy between ch solutions and cs solutions is much smaller than between hh solutions and hs solutions in their bistable range and this results in flatter fronts for the associated Ginzburg–Landau system, which we discuss in more detail in §3.2.

However, here increasing the domain gives bifurcation points on cb (e.g., 4 on a 12×2 domain), and branches connecting the first and the last, the second and the second to last, and so on, as in [Daw09], but no snaking. The reason is most likely an exponentially small width of the snaking region, which cannot be resolved by our numerics, analogous to a number of results for the qcSHe (1) and the cqSHe (2), which can directly be related to Fig. 11. For instance, [LSAC08, Fig.33,34], see also [ALB⁺10, Fig.22], show the (numerically calculated) positions of the left $\lambda_-(\nu)$ and right folds $\lambda_+(\nu)$ in the snake of hexagons over $u = 0$ in (1). Then, as expected, $\lambda_-(\nu) < \lambda_M(\nu) < \lambda_+(\nu)$, where $\lambda_M(\nu)$ is the relevant Maxwell point, but the width $s(\nu) = \lambda_+(\nu) - \lambda_-(\nu)$ goes to 0 quickly as ν becomes small, and the snaking cannot be continued down to $\nu = 0$. Analytically,

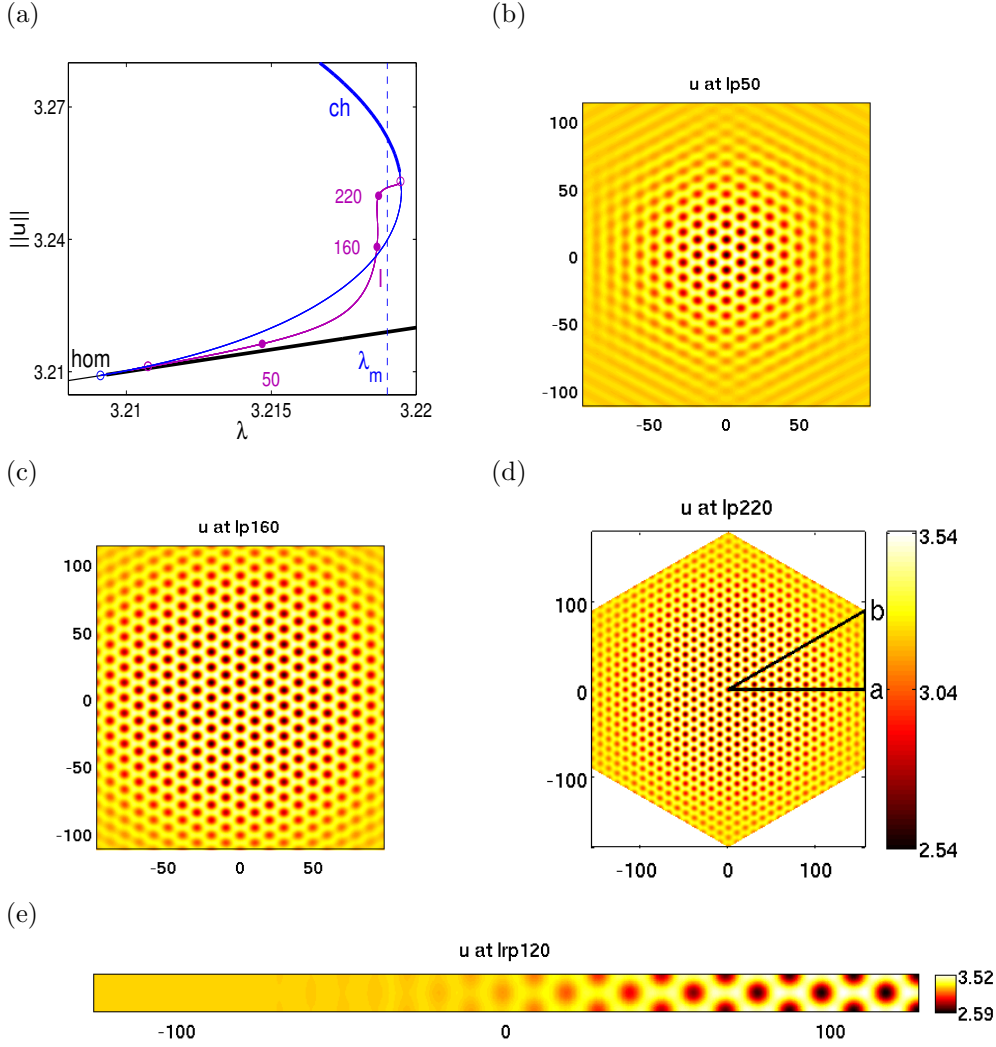


Figure 11: Bistable range between homogeneous solution and cold hexagons. (a) partial bifurcation diagram and the homogeneous Maxwell point (see §3). Additional to quasi 1D solutions we find fully 2D localized hexagon patches. The triangle in (d) indicates the computational domain with $a = (32\pi/k_c, 0)$ and $b = (32\pi/k_c, 32\pi/(\sqrt{3}k_c))$, and about 90.000 triangles. We use Neumann BC on all three sides and for plotting first make an even extension over $y = 0$ and then five rotations by 60 degrees. (e) Quasi 1D front between $w^* = (\lambda, 1/\lambda)$ and spots on a 13×1 domain, $\lambda \approx 3.219$. See [UW13] for a movie.

[CK09, SM11, DMCK11, KC13] explain that the pertinent small parameter in (1) and (2) is the subcriticality $\varepsilon(\nu) = \lambda_c - \lambda_f(\nu)$, where $\lambda_c = 0$ and $\lambda_f(\nu) < 0$ denotes the position of the fold where the subcritical rolls become stable. Formulas for $s(\varepsilon) = \lambda_+(\varepsilon) - \lambda_-(\varepsilon)$ can then be derived using beyond all order asymptotics, and show the exponential smallness of $s(\varepsilon)$ in ε , i.e.,

$$s(\varepsilon) \sim C\varepsilon^{-\alpha} \exp(-\beta/\varepsilon) \text{ as } \varepsilon \rightarrow 0, \quad (10)$$

where $C, \alpha, \beta > 0$ are numerical constants depending on the parameters of the problem and, e.g., front orientation, but not on ε . These formulas show good agreement with numerical simulations, see, e.g., [KC06, Fig.2], [DMCK11, Fig.5], [SM11, Fig.1(c)], [KC13, Fig.2,3].

If we also assume a dependence like (10) here, with $\varepsilon = \lambda_s^b - \lambda_{ch}^e \approx 0.12$ the “bistability width” of stripes and cold hexagons in Fig. 10, and $\varepsilon = \lambda_{ch}^b - \lambda_c \approx 0.02$ the subcriticality in Fig. 11, then the snaking width might be too small to resolve numerically. In fact, increasing the domain size and keeping the discretization reasonably fine, the steep part near λ_m becomes steeper, but in our

numerics this process converges to a monotonous in λ branch. To elaborate this we set up the modification (7) which for $\sigma < 0$ increases the subcriticality of the cold hexagons. See §3.3 where we find snaking of the analoga of the **c1**, and **1** branches of Fig. 10 and 11, respectively.]

2.5 Sideband patterns

By our choice of $l_1 \times l_2$ domains $\Omega = \left(-\frac{2l_1\pi}{k_c}, \frac{2l_1\pi}{k_c}\right) \times \left(-\frac{2l_2\pi}{\sqrt{3}k_c}, \frac{2l_2\pi}{\sqrt{3}k_c}\right)$ with homogeneous Neumann boundary conditions, in a neighborhood of $(w, \lambda) = (0, \lambda_c)$ *only* patterns with basic wave vectors $k_c(1, 0)$ and $k_c(-\frac{1}{2}, \pm\frac{\sqrt{3}}{2})$ exist, as these are the only unstable modes that fit into the domain. However, for larger $\lambda_c - \lambda$ more modes become unstable and hence patterns with sideband wave vectors like $k = k_c(\frac{4l_1+m_1}{4l_1}, 0)$, $m_1 = \pm 1, \pm 2, \dots$ (sideband stripes), or $k = k_c(-\frac{1}{2}\frac{4l_1+m_1}{4l_1}, \pm\frac{\sqrt{3}}{2}\frac{4l_2\pm m_2}{4l_2})$, $m_{1,2} = \pm 1, \pm 2, \dots$ (with $\|(\frac{1}{2}\frac{4l_1+m_1}{4l_1}, \frac{\sqrt{3}}{2}\frac{4l_2\pm m_2}{4l_2})\|$ close to unity to build sideband hexagons) come into play: branches of solutions with such modes bifurcate from the homogeneous branch below λ_c and should be expected to behave roughly similar as the basic stripe and hexagon branches, i.e., for $\lambda < \lambda_c$ we get an existence balloon of patterns. Moreover, although unstable at bifurcation they may become stable away from bifurcation, forming the so called Busse balloon as a subset of the existence balloon. Of course, all this heavily depends on the size of the domain: for instance, on the $2 \times l_2$ domain, the sideband (vertical) stripes have wave vectors $(k_1, 0)$ with $k_1/k_c = \frac{1}{4}, \frac{1}{2}, \frac{3}{4}, \frac{5}{4}, \dots$, while on the $8 \times l_2$ domain we have $k_1/k_c = \dots, \frac{15}{16}, \frac{31}{32}, \frac{33}{32}, \frac{17}{16}, \dots$, where for instance we call the stripe with expansion $A \sin(\frac{31}{32}k_c x) + \text{h.o.t.}$ an odd stripe, in contrast to the even stripes considered so far.

Just as an indication of how such sideband patterns can further complicate the bifurcation diagram of (4), in Fig. 12 we plot a number of “sideband” branches and sample solutions on the 8×2 domain, thus allowing many more wave numbers $k_1 = 0, \frac{1}{32}k_c, \frac{2}{32}k_c, \dots$ in x direction than wave numbers $k_2 = 0, \frac{1}{4}k_c, \dots$ in y direction. The branches **s1**, **s2** belong to (hot) “subharmonic” stripes with $k_1 = \frac{30}{32}k_c, \frac{31}{32}k_c$, respectively. Interestingly they stay stable much longer than the basic hot stripe branch **hs** which loses stability at $\lambda = \lambda_s^e \approx 2.51$. However, this is not a contradiction as k_c need not be in the Busse balloon of stable wavenumbers for $|\lambda - \lambda_c| = \mathcal{O}(1)$, see, e.g., [DRvdS12] for an interesting example.

In contrast to the **hs** branch, when losing stability, the bifurcation is no longer to beans, but directly to a localized branch **1** in case of **s1** and to a front branch **f** in case of **s2**. For **s1**, an explanation is that hot hexagons with k_1 wave numbers $\frac{15}{32}k_c$ do not exist for $\lambda > \lambda_h \approx 2.35$: for $\lambda = 2.3$ we can generate such hexagons from a suitable initial guess and time-integration, see §2.3, but as we try to continue the **h1** branch to larger λ we get a fold at λ_h , and on the lower branch the hexagons lose their shape as λ increases again. This is a finite size effect, in particular of the rather small size in y . The wave vector $k_{h1} = k_c(-\frac{15}{32}, \pm\frac{\sqrt{3}}{2})$ of the **h1** branch which yields the slightly distorted hexagons shape is the one with $|k|$ closest to k_c in the family $k = k_c(\frac{15}{32}, \frac{\sqrt{3}}{2}\frac{8\pm m_2}{8})$, and apparently this is not yet in the existence balloon for $\lambda > \lambda_h$. Consequently, we should not expect beans involving k_{h1} for $\lambda > \lambda_h$, and this explains the direct bifurcation from the **s1** branch to the **1** branch.

Similar remarks apply to the bifurcation from the **s2** branch to the **f** branch, where moreover no hexagons with $k = k_c(-\frac{31}{64}, \pm\sqrt{3}/2)$ exist on the 8×2 domain at all, for any λ in the depicted range. Thus, bifurcation to the **f** branch is the natural candidate, and by mirroring solutions over the left or right boundary this corresponds to an **1** branch over the 16×2 domain. On both snakes the segments pointing north-west are stable, and there are bifurcation points near the folds. Also note that point 200 on the **1** branch has stripes on a hexagon background and thus is already on the “way back” to the bifurcation point of **1** from **s1**. Here we close our brief discussion of 2D sideband patterns, but refer to §3.4 for (1D) branches connecting different wave numbers, and to §4.3 for fully localized sideband hexagons over stripes.

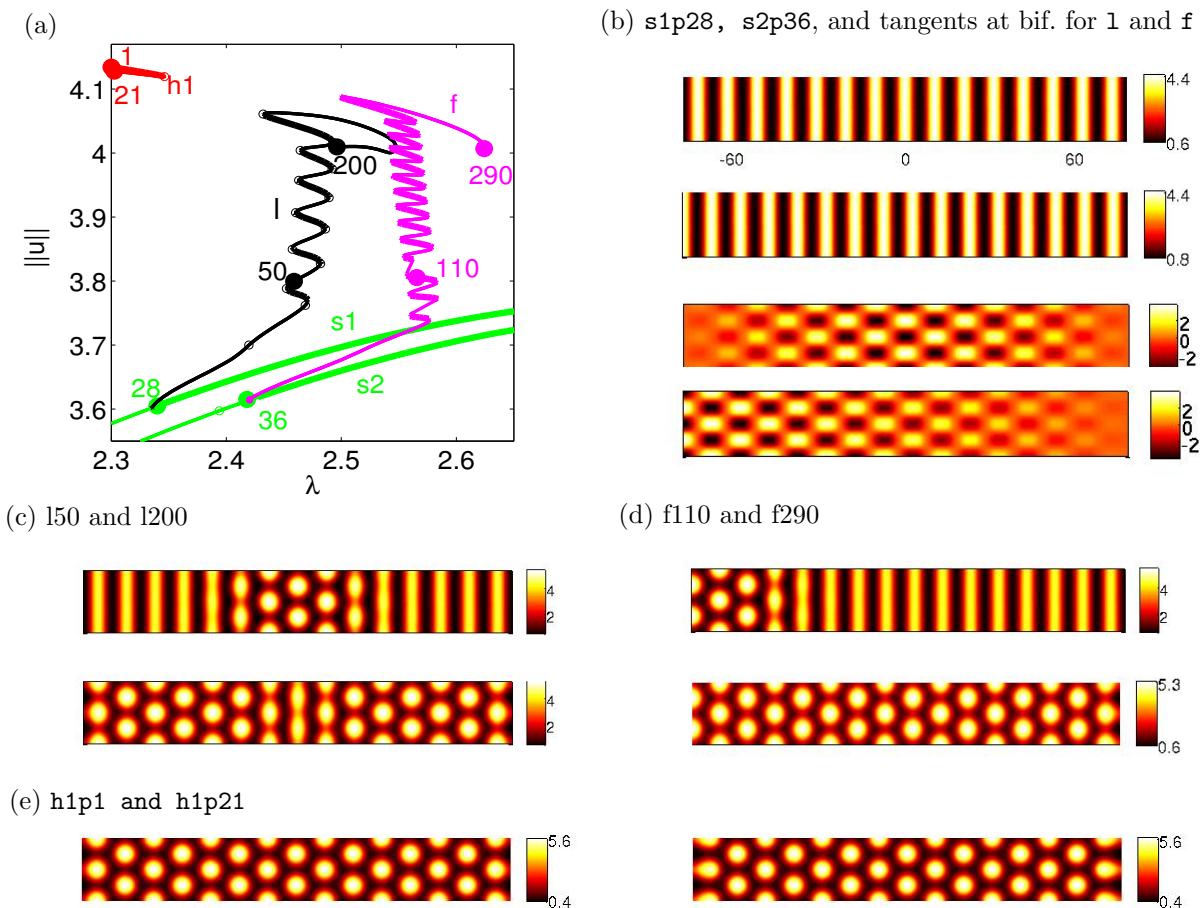


Figure 12: (a) Bifurcation diagram for patterns with sideband wavenumbers on the 8×2 domain. (b) Stripes with $k_1 = \frac{15}{16}k_c$ (s1) and $k_1 = \frac{31}{32}k_c$ (s2), and bifurcation directions from these. (c),(d) Some example plots on the bifurcating branches. (e) Slightly distorted hexagons with $k_1 = \frac{15}{16}k_c$, obtained from an initial guess and time integration followed by a Newton loop at $\lambda = 2.3$. See [UW13] for a movie.

3 Ginzburg-Landau reduction

We now approximate the hexagons, stripes and mixed modes by the Landau formalism, and the fronts and localized patterns with planar interfaces by the Ginzburg–Landau formalism. In particular, using an energy argument and the so called Maxwell point for the Ginzburg–Landau system we find an approximate prediction where to find the respective branches in the bifurcation diagram for (4). Similar ideas are worked out much more deeply for the 1D quadratic–cubic SHe (1) in [CK09] (see also [KAC09]) and the cubic–quintic SHe (2) in [DMCK11], where, by augmenting the Ginzburg–Landau ansatz with beyond all order asymptotics, accurate bifurcation diagrams for homoclinic snaking were rigorously derived.

In our case we need a system of Ginzburg–Landau equations, and our analysis is more formal since even a consistent derivation of the Ginzburg–Landau system is difficult as we refrain from scaling assumptions for quadratic interactions but rather work with the numerical coefficients in (4). However, from the Ginzburg–Landau system we calculate the Maxwell point as a necessary condition for Ginzburg–Landau fronts, and the pinning argument from [Pom86] then suggest the existence of stationary fronts for (4). This approximation turns out to be qualitatively and at least in the cold regime also quantitatively correct, and thus it gives a lowest order approximation for the numerical solutions, although it cannot explain the snaking (or the non–snaking).

In a second step we use the Ginzburg–Landau formalism as a predictive tool to choose the σ direction in the modified model (7) in which we can increase the subcriticality of the cold regime

to obtain cold snaking branches (§3.3), and in which we have subcritical bifurcation of stripes and hence can expect 1D snaking (§3.4).

3.1 Landau description of hexagons, stripes, and mixed modes

To formally describe planar fronts for (4) by a Ginzburg-Landau system the idea is to treat x as an unbounded variable, while $y \in [-\frac{m\pi}{\sqrt{3}k_c}, \frac{m\pi}{\sqrt{3}k_c}]$ with Neumann boundary conditions, as in the numerics. At least close to λ_c the most unstable modes of the linearization $L(\Delta)$ of (5) around 0 are then $e_1\Phi$, $e_2\Phi$, and $e_3\Phi$, where $e_1 = e^{ik_c x}$, $e_2 = e^{ik_c(-x+\sqrt{3}y)/2}$, $e_3 = e^{ik_c(-x-\sqrt{3}y)/2}$, and $\Phi = \Phi(\lambda) \in \mathbb{R}^2$ is the eigenvector of $\hat{L}(k_c, \lambda)$ to the eigenvalue $\mu_+(k_c, \lambda)$. First we consider slowly varying complex amplitudes $A_j = A_j(t)$ of these modes, $j = 1, 2, 3$, i.e., our ansatz reads

$$w = \sum_{i=1}^3 A_i e_i \Phi + \frac{1}{2} \sum_{i=1}^3 |A_i|^2 \phi_0 + \sum_{i=1}^3 A_i^2 e_i^2 \phi_1 + \sum_{1 \leq i < j \leq 3} A_i \bar{A}_j e_i \bar{e}_j \phi_2 + \text{c.c.} + \text{h.o.t.}, \quad (11)$$

where \bar{A}_j means the complex conjugate of A_j , c.c. stand for the complex conjugate of all preceding terms, and h.o.t. stands for higher order terms. This is taken as a weakly nonlinear expansion, i.e., the goal is to successively remove terms of order A_j^m , $m = 1, 2, 3$ from the residual $L(\Delta)w + G(w)$, where the amplitudes A_j are assumed to be small, though later we will use the expansion also for $\mathcal{O}(1)$ amplitudes. The vectors ϕ_0 , ϕ_1 , and ϕ_2 are introduced to remove quadratic terms at wave vectors \mathbf{k} with $k = |\mathbf{k}| = 0$, $k = 2k_c$ and $k = \sqrt{3}k_c$ from the residual.

The calculations are best organized by writing (5) in the form

$$\partial_t w = L(\Delta)w + B(w, w) + C(w, w, w), \quad (12)$$

where B and C are symmetric bilinear and trilinear forms. To remove terms of order $A_i A_j$ from (4) we need

$$\begin{aligned} \phi_0(\lambda) &= -2\hat{L}(0, \lambda)^{-1}B(\Phi, \bar{\Phi}), & \phi_1(\lambda) &= -\hat{L}(2k_c, \lambda)^{-1}B(\Phi, \Phi), \\ \phi_2(\lambda) &= -2\hat{L}(\sqrt{3}k_c, \lambda)^{-1}B(\Phi, \bar{\Phi}). \end{aligned} \quad (13)$$

These terms arise due to quadratic interactions of the forms, e.g., $B(A_1 e_1 \Phi, \overline{A_1 e_1 \Phi}) = |A_1|^2 B(\Phi, \bar{\Phi})$, $B(A_1 e_1 \Phi, A_1 e_1 \Phi) = A_1^2 e^{2ik_c x} B(\Phi, \Phi)$, and $B(A_1 e_1 \Phi, \overline{A_2 e_2 \Phi}) = A_1 \bar{A}_2 e^{i\frac{k_c}{2}(3x-\sqrt{3}y)} B(\Phi, \bar{\Phi})$. Although $\Phi \in \mathbb{R}^2$ in our case we keep the notation $\bar{\Phi}$ as this makes it easier to see where the respective terms come from. The matrices $\hat{L}(0, \lambda)$, $\hat{L}(2k_c, \lambda)$ and $\hat{L}(\sqrt{3}k_c, \lambda)$ are invertible at least for λ not too far from λ_c . From the Fredholm alternative we obtain the Landau ODE system as the solvability conditions for removing terms up to cubic order at the critical modes, namely

$$\begin{aligned} \text{at } e_1 : \quad \partial_t A_1 &= f_1(A_1, A_2, A_3) := c_1 A_1 + c_2 \overline{A_2 A_3} + c_3 |A_1|^2 A_1 + c_4 A_1 (|A_2|^2 + |A_3|^2), \\ \text{at } e_2 : \quad \partial_t A_2 &= f_2(A_1, A_2, A_3) := c_1 A_2 + c_2 \overline{A_1 A_3} + c_3 |A_2|^2 A_2 + c_4 A_2 (|A_1|^2 + |A_3|^2), \\ \text{at } e_3 : \quad \partial_t A_3 &= f_3(A_1, A_2, A_3) := c_1 A_3 + c_2 \overline{A_1 A_2} + c_3 |A_3|^2 A_3 + c_4 A_3 (|A_1|^2 + |A_2|^2), \end{aligned} \quad (14)$$

with $c_1(\lambda) = \mu_+(k_c, 0, \lambda)$, $c_2(\lambda) = 2\langle B(\bar{\Phi}, \bar{\Phi}), \Phi^* \rangle$, $c_3(\lambda) = \langle 3C(\Phi, \Phi, \bar{\Phi}) + 2B(\bar{\Phi}, \phi_1) + 2B(\Phi, \phi_0), \Phi^* \rangle$, and $c_4(\lambda) = \langle 6C(\Phi, \Phi, \bar{\Phi}) + 2B(\Phi, \phi_2) + 2B(\Phi, \phi_0), \Phi^* \rangle$. Here $\Phi^*(\lambda)$ is the adjoint eigenvector of $\hat{L}(k_c, \lambda)$ to the eigenvalue $\mu_+(k_c, \lambda)$, normalized such that $\langle \Phi, \Phi^* \rangle = 1$. At \bar{e}_j , $j = 1, 2, 3$, we obtain the complex conjugate equations. See, e.g., [GSK84, Pom86], [CH93, §IV,A,1,a(iii)], [DSSS03, §2], [Hoy06, §5], [NG06, Pis06], which also explain that (14) is the generic form of the amplitude equations for hexagonal symmetry. The next step is the actual calculation of the coefficients.

Remark 3.1. In (11), $\Phi = \Phi(k_c, \lambda)$ varies with λ and is not fixed at $\lambda = \lambda_c$, which would be the more classical ansatz. Similarly, terms like (13) and the coefficients c_2, \dots, c_4 are evaluated at λ ,

not as usual at $\lambda = \lambda_c$. The formalisms are equivalent for $\lambda \rightarrow \lambda_c$ with the differences hidden in the h.o.t. in (11). The reason why we always evaluate at λ is that we want to use the formalism also for $\lambda_c - \lambda = \mathcal{O}(1)$ and then expect (and find) better approximations with $\Phi = \Phi(\lambda)$. On the other hand, for the comparison with the numerics we want to keep the wave vectors fixed and thus evaluate at k_c , which approximately stays the most unstable wave number also for $\lambda_c - \lambda = \mathcal{O}(1)$.]

From the coefficients $c_j(\lambda)$, $j = 1, \dots, 4$, see Fig. 13(a), it follows that

$$T_{\pm} = \pm \sqrt{-\frac{c_1}{c_3}} \quad \text{and} \quad P_{\pm} = -\frac{c_2}{2(c_3 + 2c_4)} \pm \sqrt{\frac{c_2^2}{4(c_3 + 2c_4)^2} - \frac{c_1}{c_3 + 2c_4}}, \quad (15)$$

are real in the Turing-unstable range $\lambda < \lambda_c$, respectively for $\lambda < \lambda_{\text{GLfold}} \approx \lambda_{cb} \approx 3.22$. The triples $(T_+, 0, 0)$, $(T_-, 0, 0)$, (P_+, P_+, P_+) , and (P_-, P_-, P_-) solve (14) and via (11) generate hot stripes, cold stripes, hot hexagons, and cold hexagons, respectively. Mixed modes are obtained from setting $A_3 = A_2$ and solving (14) for (A_1, A_2) .

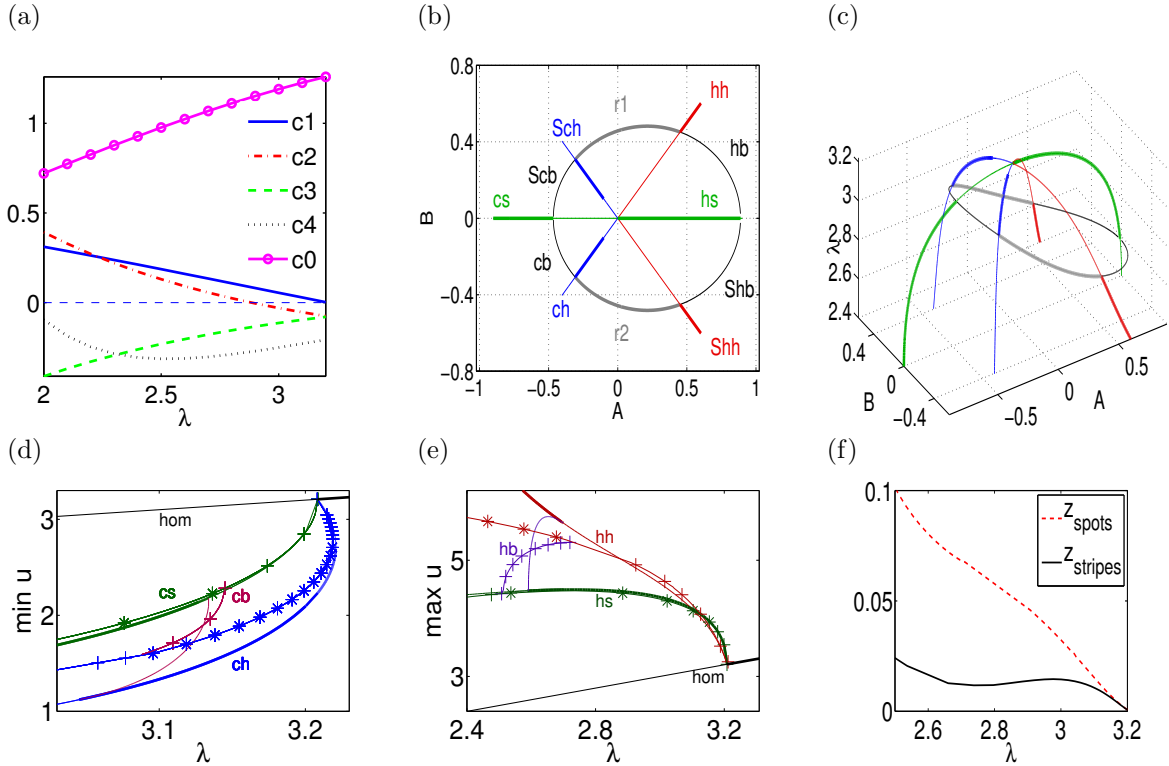


Figure 13: (a) Landau coefficients, and Ginzburg–Landau coefficient c_0 , see §3.2. (b),(c) Landau bifurcation diagram in the invariant subspace $A_1 =: A \in \mathbb{R}$ and $A_2 = A_3 =: B \in \mathbb{R}$, stability/instability indicated by thick/thin lines. (d),(e) Comparisons of numerical bifurcation diagram from Fig. 3 (indicated by * for stable points and + for unstable points) with Landau bifurcation diagram near the cold and hot bistable regimes. (f) relative L^1 errors between hot numerical and Landau solutions defined in (16).

The formulas, together with the signs of $c_j(\lambda)$, also explain the supercritical pitchfork bifurcation of stripes, and the transcritical bifurcation of the hexagons. Figures 13(b),(c) show the complete bifurcation diagram for stationary solutions of (14) in the invariant subspace $A_1 =: A \in \mathbb{R}$ and $A_2 = A_3 =: B \in \mathbb{R}$, while (d),(e) compares the bifurcation diagram of stripes, hexagons and beans for (14) with the numerical bifurcation diagram from Fig. 3 for the full system (4). Though qualitatively correct down to $\lambda = 2.4$, the approximation errors grow with $|\lambda - \lambda_c|$, as expected. Additionally to the L^∞ like error already shown, for $i \in \{\text{stripes, hexagons}\}$ we define the relative

L^1 errors

$$z_i = \frac{\sum_{(x,y) \in \Omega_d} \|U_{\text{num},i}(x,y) - U_i(x,y)\|_1}{\sum_{(x,y) \in \Omega_d} \|U_{\text{num},i}(x,y)\|_1} \quad (16)$$

between the numerical solutions U_{num} and approximate solutions $U = w^* + w$ from (11), where Ω_d is the discretization used to calculate the numerical solution from Fig. 3. It turns out that z_{stripes} stays rather small also for $\lambda_c - \lambda = \mathcal{O}(1)$, while z_{hex} behaves worse, see Fig. 13(f), and also Remark 3.2 for further comments.

Another notable discrepancy between the Landau bifurcation diagram and the (numerical) bifurcation diagram for (4) is that in the former the (hot) stripes are stable all the way to the bifurcation point, while in the PDE this depends on the domain size. On a 1×1 domain we obtain exactly the same stability as displayed in Fig. 13(b),(c), and the instability near bifurcation of the stripes already on a 2×2 domain as in Fig. 3 is due to a long zig-zag instability, which is not captured in our Landau ansatz. Similar remarks apply for instance to the rectangle branches, which are mostly unstable for (4) over a 2×2 domain.

3.2 Ginzburg–Landau formalism and fronts

Motivated by the acceptable approximation of the hexagons, stripes and beans via (11) and (14) we proceed to use the Ginzburg–Landau (GL) reduction to predict the stationary fronts and localized patterns. If instead of $A_j = A_j(t)$ we assume that $A_j = A_j(t, x)$ are slowly varying functions also of $x \in \mathbb{R}$, then instead of the Landau system (14) we obtain the Ginzburg–Landau system

$$\partial_t A_1 = c_0 \partial_x^2 A_1 + f_1(A_1, A_2, A_3), \quad \partial_t A_j = \frac{c_0}{4} \partial_x^2 A_j + f_j(A_1, A_2, A_3), \quad j = 2, 3, \quad (17)$$

where $c_0(\lambda) = -\frac{1}{2} \partial_{k_1}^2 \mu_+((k_c, 0), \lambda) > 0$. See [Sch94, BvHS95, Sch99, Mie02] for background on this formal procedure, and for so called attractivity and approximation theorems which estimate the difference between a true solution of (3) and an approximation described by (11) and (17), close to bifurcation. These theorems involve some small amplitude assumption for (u, v) , related slow scales for t and x in $A_j(t, x)$, and, for the present case of three resonant modes, a suitable scaling for the quadratic interactions, i.e., small c_2 .

Here we again want to use the GL system (17) at an $\mathcal{O}(1)$ distance from λ_c and find a necessary condition for stationary fronts between hexagons like $A \equiv (P_+, P_+, P_+)$ and stripes like $A \equiv (T_+, 0, 0)$ in (17). Thus we consider the stationary Ginzburg–Landau system

$$c_0 \partial_x^2 A_1 + f_1(A_1, A_2, A_3) = 0, \quad \frac{c_0}{4} \partial_x^2 A_j + f_j(A_1, A_2, A_3) = 0, \quad j = 2, 3, \quad (18)$$

as a dynamical system in the spatial variable x . Now restricting to real amplitudes A_j , the total energy of (18) is given by $E_{\text{total}} = E_{\text{kin}} + E_{\text{pot}}$, where

$$E_{\text{kin}} = \frac{c_0}{2} \left((\partial_x A_1)^2 + \frac{1}{4} (\partial_x A_2)^2 + \frac{1}{4} (\partial_x A_3)^2 \right), \quad \text{and}$$

$$E_{\text{pot}} = \sum_{i=1}^3 \left(\frac{c_1}{2} A_i^2 + \frac{c_3}{4} A_i^4 \right) + c_2 A_1 A_2 A_3 + \frac{c_4}{2} (A_1^2 A_2^2 + A_1^2 A_3^2 + A_2^2 A_3^2)$$

are the kinetic and potential energy, respectively. Then $\frac{d}{dx} E_{\text{total}} = 0$, i.e., E_{total} is conserved. Thus, a necessary condition for, e.g., a heteroclinic orbit A_{front} between (P_+, P_+, P_+) and $(T_+, 0, 0)$ to exist in (18) is $E_{\text{pot}}(T_+, 0, 0) = E_{\text{pot}}(P_+, P_+, P_+)$. Again we first focus on the hot bistable range and in Fig. 14(a) plot $E_{\text{pot}}(T_+, 0, 0)$ and $E_{\text{pot}}(P_+, P_+, P_+)$. Their intersection defines the so called (hot) Maxwell point λ_m . Though we refrain from discussing the general energy landscape and

dynamics of (18), it turns out that at least numerically the necessary condition $\lambda = \lambda_m$ is also sufficient. Figure 14(b) shows a stationary front for (17) (with Neumann boundary conditions), which can either be obtained from time evolution of (17) with a suitable initial guess, or from solving the stationary boundary value problem. See also [MNT90] for some more analysis for front solutions of (18), including some implicit solution formulas. On the other hand, for $\lambda < \lambda_m$ with $E_{\text{pot}}(T_+, 0, 0) < E_{\text{total}}(P_+, P_+, P_+)$ we obtain a front for (17) *travelling* towards higher energy, i.e., (P_+, P_+, P_+) invades $(T_+, 0, 0)$, and vice versa for $\lambda > \lambda_m$.

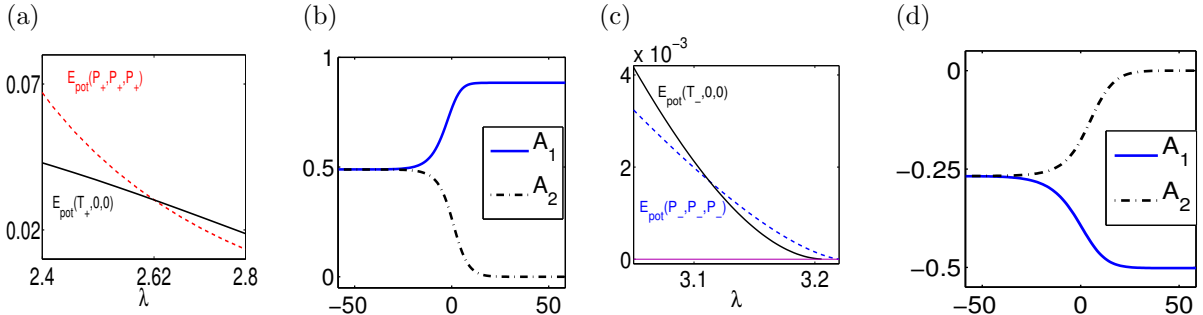


Figure 14: (a), (c) Energies of hexagons and stripes near the hot resp. cold bistable regimes; their intersections define the respective Maxwell points $\lambda = 2.62$, $\lambda = 3.11$, and the zero of $E_{\text{pot}}(P_-, P_-, P_-)$ defines the third Maxwell point $\lambda = 3.219$. Hot (b) and cold (d) stationary Ginzburg–Landau fronts between stripes and hexagons at the respective Maxwell points, for comparison both over domain $[-12\pi/k_c, 12\pi/k_c]$, $A_3 = A_2$.

Thus, from the GL approximation *standing* fronts U_{het} between different patterns are only predicted at precisely $\lambda = \lambda_m$. In the physics literature, e.g., [Pom86], the basic argument for the existence of U_{het} in an interval around λ_m is that the patterns create an effective periodic potential which yields a pinning of fronts.

It is not obvious whether the stationary GL system (18) has homoclinic solutions A_{hom} with, say, $A_{\text{hom}}(x) \rightarrow (P_+, P_+, P_+)$ as $x \rightarrow \pm\infty$, and that pass near $(T_+, 0, 0)$ near $x = 0$. However, (suitably shifted) fronts $A_{\text{front}}(x_0 + \cdot)$ and “backs” $A_{\text{back}}(x_1 + \cdot)$ with $A_{\text{back}}(x) = A_{\text{front}}(-x)$ can be glued together to give approximate homoclinics with long plateaus but also with some dynamics in time which can be expected to be exponentially slow in the separation distance between A_{front} and A_{back} , see, e.g., [CP90]. In fact we can generate almost stationary pulses numerically, but eventually the solution decays to a homogeneous rest state $(T_+, 0, 0)$ or (P_+, P_+, P_+) . Similarly, (18) may have periodic orbits which stay close to (P_+, P_+, P_+) resp. $(T_+, 0, 0)$ over very long x -intervals. Clearly, for these “approximate homoclinics” a similar pinning argument as for the heteroclinics should apply and predict the existence of localized patterns as in Fig. 5 near the Maxwell point λ_m .

In [CK09, DMCK11] it is worked out mathematically that the pinning and hence also the snaking are exponentially small effects and thus cannot be predicted at any order by Ginzburg–Landau type asymptotic expansions alone. However, as already indicated in Remark 2.5, using beyond all order asymptotics snaking in the model problems (1) and (2) can be described very accurately. See also, e.g., [Kno08, ALB⁺10] and the references therein for alternative arguments explaining the snaking via so called heteroclinic tangles in the spatial dynamics formulation of again (1) and (2).

The same pinning arguments apply to the cold bistable range (Fig. 10), but the difference to the hot range is that the bistability resp. subcriticality as measured by ε in Remark 2.5 in the cold range is much smaller than in the hot range. Here we repeat, from a slightly different point of view, the heuristic argument, why this makes the snaking region very small and thus snaking impossible to detect in our numerics. Small ε in the cold range relates to the fact that the dependence of $|E_{\text{pot}}(T_-, 0, 0) - E_{\text{pot}}(P_-, P_-, P_-)|$ on λ in the cold range is much flatter than that of $|E_{\text{pot}}(T_+, 0, 0) - E_{\text{pot}}(P_+, P_+, P_+)|$ on λ in the hot range. A short calculation then yields that relatively to the diffusion constant c_0 the vector fields f_1, f_2 in (18) are smaller in the cold range

than in the hot range. Therefore, cold Ginzburg–Landau fronts are flatter and wider than hot ones, cf. Fig. 14(b) and (d). Thus, if for convenience we write $u(x, y; \lambda) = \sum_{j=1}^3 A_j(\varepsilon x; \lambda) e_i \Phi(k_c) + \text{c.c.}$ for a localized pattern u , assuming that the A_j vary on an $\mathcal{O}(1)$ scale, then there is a stronger separation of scales in the cold range than in the hot range. Consequently, in the cold range the Fourier transform of u in x is more localized around the pertinent k_j due to

$$\hat{u}(k, y; \lambda) = \frac{1}{\varepsilon} \left(\sum_{j=1}^3 \hat{A} \left(\frac{k - k_j}{\varepsilon}; \lambda \right) e^{il_j y} + \text{c.c.f.} \right) \Phi(k_c), \quad (19)$$

where $k_1 = k_c$, $k_{2,3} = -\frac{1}{2}k_c$, $l_1 = 0$, $l_{2,3} = \pm \frac{\sqrt{3}}{2}$.

On the other hand, repeating the Ginzburg–Landau analysis leading to (17) with the x -wave number k as a parameter, $k \approx k_c$, we obtain a wave number dependent Ginzburg–Landau energy $E_{\text{total}}(\lambda, k)$ for patterns. Then $\frac{d}{dx} E_{\text{total}} = 0$ along a localized pattern can be seen as a selection principle for the average wave number k , or conversely defines a function $\lambda = \lambda(k)$ with generically $\lambda'(k) \neq 0$, see, e.g., [BD12]. Therefore, if $\hat{u}(k; \lambda)$ is only weakly localized in the different k_j (i.e., ε not very small in (19)), then we expect a strong λ dependence in the branch of localized patterns, and hence that λ varies over a significant range during growth of a localized pattern, and we may expect λ to snake back and forth during that growth. Conversely, for small ε in (19) we expect a narrow λ range for some growing pattern, as in Fig. 10 and 11, and snaking is difficult to detect numerically. See also §3.3 for more quantitative arguments.

Remark 3.2. An ad hoc way to derive a Landau system like (14) from a system like (4) is to *only* consider the solvability conditions (14) at the critical modes without first removing the A^2 residual at second harmonics. This amounts to the *first order ansatz* $w = \sum_{i=1}^3 A_i e_i \Phi + \text{c.c.}$, or in other words setting $\phi_0, \phi_1, \phi_2 = 0$ in (13). We denote the new coefficients in (14) by c_{31} and c_{41} . This is obviously simpler than (11), but not formally consistent. However, at order $\mathcal{O}(1)$ distance from the bifurcation the first order ansatz *may* give a better approximation of solutions than the ansatz (11), since (11) represents only an asymptotic expansion, and not the first terms in some convergent series.

It turns out that in some sense this is indeed the case for (4), and this can be used to improve the prediction of the Maxwell point. While in the hot bistable range the first order ansatz gives a much larger error for the stripes, its error for the hot hexagons is in fact smaller than the one in Fig. 13(c). The idea is to use the coefficients $c_3(\lambda)$ obtained from (11) for the stripes and the coefficients $c_{31}(\lambda), c_{41}(\lambda)$ from the first order ansatz for the hexagons in a “mixed” Ginzburg–Landau system that retains the variational structure. Thus, let S be T_+ and H be P_+ determined by using (11) and the first order ansatz, respectively, and consider the system

$$\begin{aligned} c_0 \partial_x^2 A_1 + c_1 A_1 + c_2 A_2 A_3 + \left(c_3 \left(\frac{A_1 - H}{S - H} \right) + c_{31} \left(\frac{A_1 - S}{H - S} \right) \right) A_1^3 + c_{41} A_1 (A_2^2 + A_3^2) &= 0, \\ \frac{c_0}{4} \partial_x^2 A_2 + c_1 A_2 + c_2 A_1 A_3 + \left(c_3 \left(\frac{A_2 - H}{S - H} \right) + c_{31} \left(\frac{A_2 - S}{H - S} \right) \right) A_2^3 + c_{41} A_2 (A_1^2 + A_3^2) &= 0, \quad (20) \\ \frac{c_0}{4} \partial_x^2 A_3 + c_1 A_3 + c_2 A_1 A_2 + \left(c_3 \left(\frac{A_3 - H}{S - H} \right) + c_{31} \left(\frac{A_3 - S}{H - S} \right) \right) A_3^3 + c_{41} A_3 (A_1^2 + A_2^2) &= 0. \end{aligned}$$

In the hot bistable range we have $S > H$ such that (20) is well-defined in this range. Moreover, (20) has again a conserved energy $E_{\text{total}} = E_{\text{kin}} + E_{\text{pot}}$ where now

$$E_{\text{pot}} = \sum_{i=1}^3 \frac{c_1}{2} A_i^2 + c_2 A_1 A_2 A_3 + \sum_{i=1}^3 A_i^4 \left(c_3 \frac{\frac{1}{5} A_i - \frac{1}{4} H}{S - H} + c_{31} \frac{\frac{1}{5} A_i - \frac{1}{4} S}{H - S} \right) + \frac{c_4}{2} (A_1^2 A_2^2 + A_1^2 A_3^2 + A_2^2 A_3^2).$$

Using this energy to calculate the hot Maxwell–point for (20) we find $\lambda_m = 2.67$ which is more in the center of the snaking region than $\lambda_m = 2.62$. Thus, using the additional information that the

hexagons are better approximated by the first order ansatz than by (11) we can obtain a better prediction for the Maxwell point.]

3.3 A modification with cold snakes and 1D snaking

In §2.4 and before Remark 3.2 we conjecture that the observed non snaking of cold connecting branches is due to the weak difference in (Ginzburg–Landau) energy of the associated patterns, which are also related to the narrow range of bistability between the cold hexagons and the cold stripes or the homogeneous solution, respectively, and which we expect to yield exponentially narrow snaking regions, cf. (10). To study this quantitatively we now consider a modification of (4). Clearly, many such modifications are possible, for instance using the Selkov–Schnakenberg parameters a, b , or varying the diffusion constant d , which we fixed to $d = 60$.

Here consider the modification (7), i.e., for the stationary case,

$$D\Delta U + N(U, \lambda) + \sigma \begin{pmatrix} u - \frac{1}{v} \\ -1 \end{pmatrix} = 0, \quad (21)$$

which has the advantage that the homogeneous solution $w = (\lambda, 1/\lambda)$, the linearization around w and thus λ_c do not depend on σ . Consequently, proceeding as in §3.2, σ only changes the Landau coefficients c_2, c_3 , and c_4 . For solutions of (14) we calculate that there is a fold on the hexagon branch if the discriminant of P_{\pm} of (15) vanishes, i.e., at

$$c_1 = c_f := \frac{c_2^2}{4(c_3 + 2c_4)}. \quad (22)$$

Let λ_f be the corresponding λ value, such that $\lambda_f - \lambda_c$ is a measure of the strength of the subcriticality on the Landau level. Near λ_c this is proportional to $-c_1$ since c_1 is essentially a linear function of $\lambda - \lambda_c$ for λ near λ_c , see Fig. 13(a). In Fig. 15(a) we plot c_f and the Landau coefficients c_2, c_3, c_4 in λ_c as functions of σ . The value $c_f(\sigma)$ and thus the subcriticality predicted by the Landau formalism increases monotonously by reducing σ from 0, and this also increases the potential energy difference for $\lambda > \lambda_c$, see Fig. 15(b). Following Remark 2.5 and the end of §3.2 this suggests that for negative σ we may find snaking branches for localized cold hexagons on the homogeneous background, and this Ginzburg–Landau prediction is confirmed numerically for the system (21) in (c), where snaking starts around $\sigma = -0.25$ and becomes stronger when further decreasing σ .

Similarly, the width of the bistable range between cold hexagons and cold stripes and the energy differences between these patterns increase with decreasing σ (Fig. 15(d),(e)). This suggest to also find snaking branches between cold hexagons and cold stripes for negative σ , and this confirmed by the numerics in (f), where again the snaking increases with decreasing σ .

For $\sigma_c \approx -0.369$ we have $c_3 + 2c_4 = 0$ and $c_f \rightarrow \mp\infty$ for $\sigma \rightarrow \sigma_c \pm 0$. Clearly, this cannot be used as a prediction of the fold position as for large $\lambda - \lambda_c$ higher order terms must be taken into account. Nevertheless, in Fig. 15(a) the plot continues down to $\sigma = -0.9$ as the sign change of c_3 near $\sigma = \sigma_0 \approx -0.3$ has another interesting consequence: for $\sigma < \sigma_0$ we have a subcritical bifurcation of stripes, and hence the possibility of 1D homoclinic snaking between stripes and the homogeneous background, which we illustrate in the next section.

Remark 3.3. (a) From $c_2(\sigma_0) = 0$ in Fig. 15(a), with $\sigma_0 \approx 0.3$, we expect a codimension 2 point for (21) at $(\lambda, \sigma) = (\lambda_c, \sigma_c)$ with $\sigma_c \approx \sigma_0$. Then a formally consistent Ginzburg–Landau expansion could be performed in (λ_c, σ_c) , which together with beyond all order asymptotics should yield a result like (10), i.e., $s(\varepsilon) = C\varepsilon^{-\alpha} \exp(-\beta/\varepsilon)$.

(b) From the subcriticality $\varepsilon(\sigma) := \lambda_f(\sigma) - \lambda_c$ and the width $s(\varepsilon)$ of the snakes in, e.g., Fig. 15(c) we could also fit the coefficients C, α, β in expansions like (10), and thus estimate the snaking width at $\sigma = 0$, and similar for the snaking between stripes and cold hexagons in Fig. 15(f). Here, however, we refrain from this, since we should first establish (10), and since even if we assume (10),

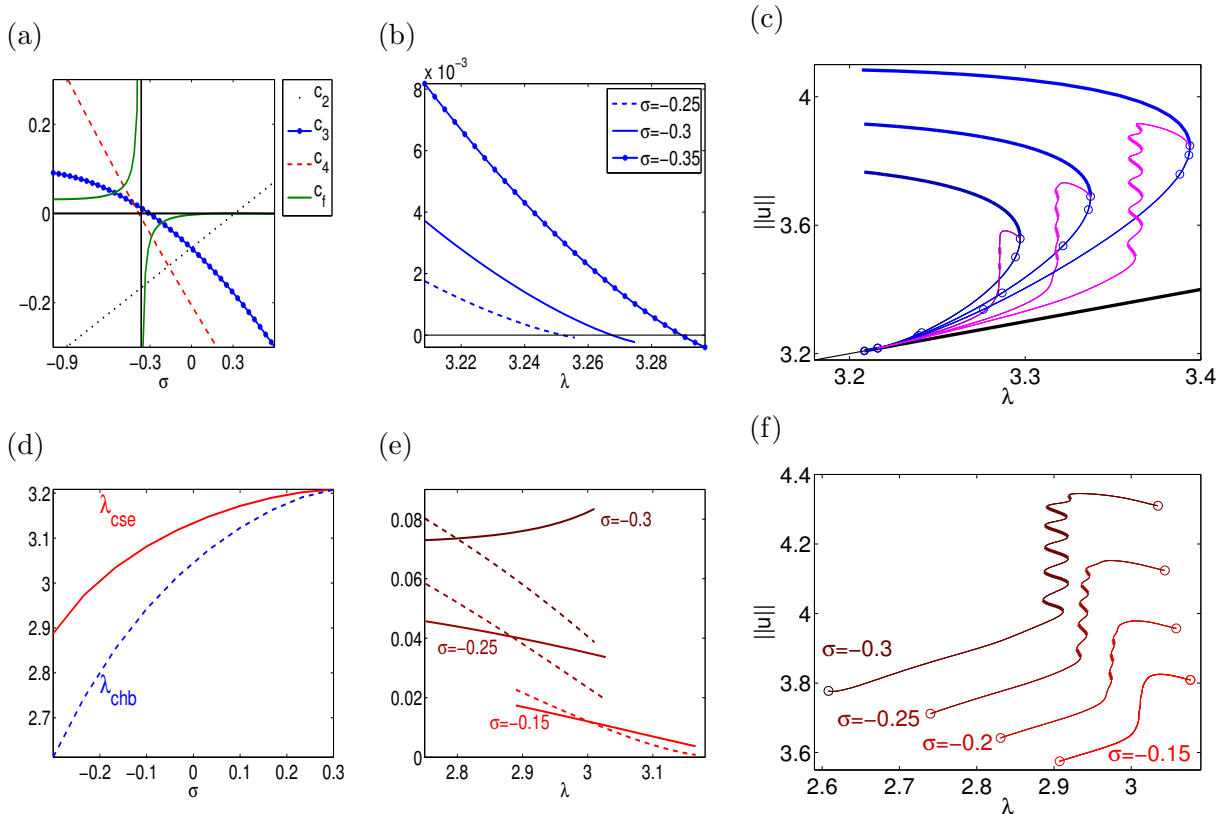


Figure 15: Switching on cold snaking for the modified model (21) by decreasing σ . (a) Landau coefficients evaluated in λ_c , and c_f , as functions of σ . (b) Potential energies of cold hexagons for different σ values. (c) Branches of localized hexagons over the homogeneous state on the 4×2 domain for $\sigma = -0.25, -0.3$, and -0.35 . (d) $\lambda_s^e(\sigma)$ and $\lambda_{ch}^b(\sigma)$ such that $\lambda_s^e - \lambda_{ch}^b$ gives the width of the bistable range of cold stripes and hexagons as a function of σ . (e) Potential energies (solid lines) of cold hexagons and stripes (dashed). (f) branches of localized patterns in bistable ranges between cold hexagons and cold stripes on the 4×2 domain.

then $\varepsilon(\sigma)$ and $s(\varepsilon)$ should be calculated numerically from fold continuation for $\lambda_f(\sigma)$ and $\lambda_{\mp}(\sigma)$, where $\lambda_{\mp}(\sigma)$ are, e.g., the first left and right folds in the snakes in Fig. 15(c). Our current version of `pde2path` does not have this fold continuation, which will however be implemented in the next version.]

3.4 1D snaking

For (3) in 1D there is no bistable range of patterns because the hexagons do not exist and stripes do not bifurcate subcritically, and thus we do not expect any localized patterns. For the modification (21) of (3) we have a bistable range: the stripes bifurcate subcritically if c_3 is positive, i.e., for $\sigma < \sigma_0 \approx -0.3$. We choose $\sigma = -0.6$ and use `pde2path` to numerically investigate (21) over the one dimensional domain $\Omega = (-8\pi/k_c, 8\pi/k_c)$, cf. Remark 2.3(d). Then the stripe patterns branch S_8 with wave number k_c and hence eight periods bifurcates in λ_c . From the second, third, and fourth bifurcation point on the homogeneous branch stripe patterns with 8.5, 7.5, and 7 (S_7 branch) periods bifurcate, respectively. We chose the rather small domain as in this section we want to give a somewhat complete picture of the secondary bifurcations on the S_8 and S_7 branches.

The first interesting observation is that the S_8 branch does not acquire stability in the fold near $\lambda \approx 3.4$, but for smaller $\lambda \approx 2.93$, see Fig.16(a), and the fold for the S_7 branch is to the right of the S_8 fold, and S_7 becomes stable in its fold. This is somewhat similar to Fig. 9 in [BBKM08] where it is illustrated that also for the 1D quadratic-cubic SHe (1) the leftmost fold does not belong to the

critical wave-number $k_c = 1$ (in that case). Moreover, from the first bifurcation point on S8 there bifurcates a snaking branch of stationary fronts F87 which however does not connect back to S8, but to the 9th bifurcation point on S7, which is close to the fold. This agrees with the heuristics that branches of localized patterns connect patterns with bistability.

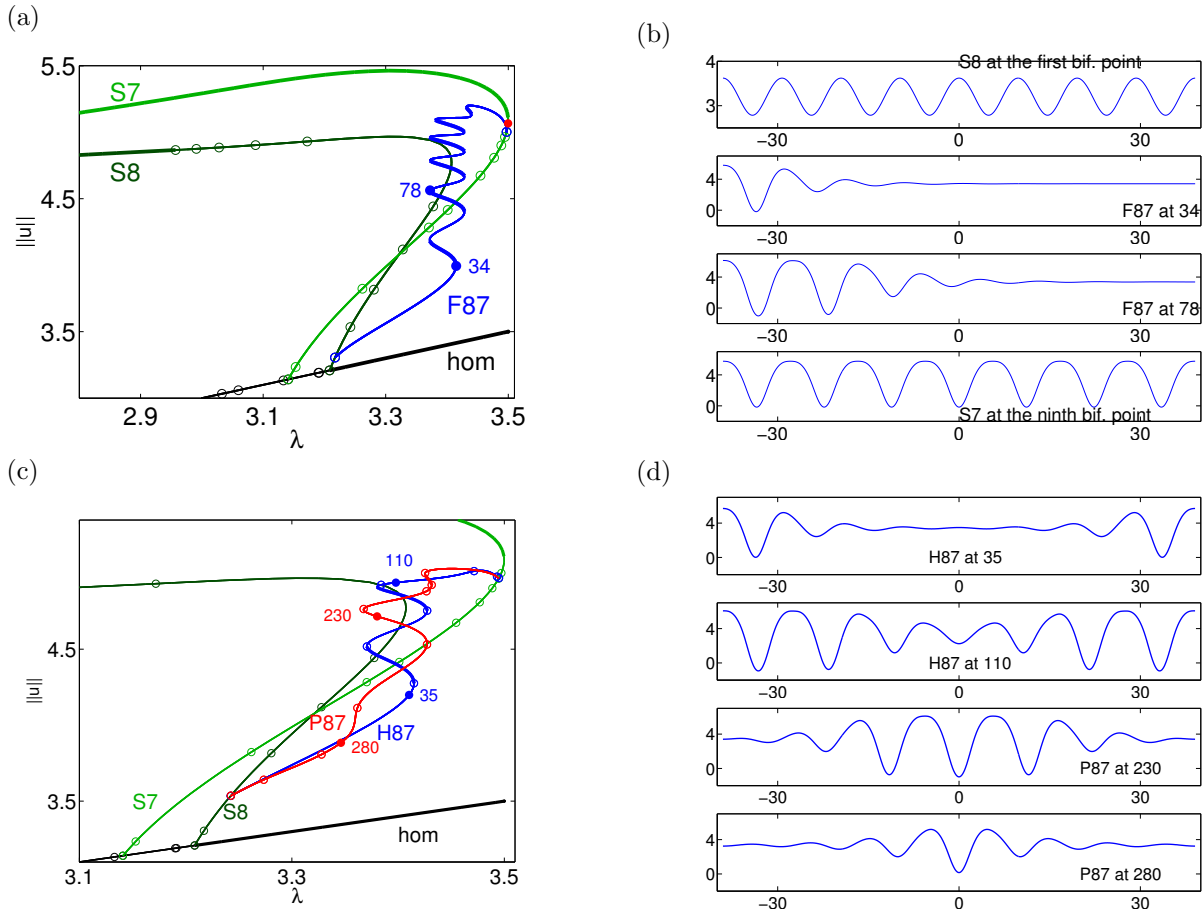


Figure 16: Two primary periodic branches S8 and S7, and branches connecting S8 and S7 for $\sigma = -0.6$ over the one dimensional domain $\Omega = (-8\pi/k_c, 8\pi/k_c)$. (a),(b) front type; (c),(d) homoclinic type. The red dot in (a) marks a Hopf point, see Remark 3.4. See also [UW13] for a movie.

Similarly, from the second bifurcation point on S8 we obtain a connecting branch to the 8th bifurcation point on S7, see Fig. 16(c),(d). In fact, here we plot the full loop connecting these points, as the way from S8 to S7, which consists of solutions with patterns at the boundary and a *hole* in the middle, is different from the way back, given by solutions with a (negative) *peak* in the middle, and these two branches are not related by symmetry.

From the third bifurcation point on S8 bifurcates a branch which connects to the S6.5 branch, i.e., a branch with 6.5 periods. The branches bifurcating from the remaining bifurcation points on S8 reconnect to S8 as illustrated in Fig. 17, and similarly bifurcation points 1-6 on S7 connect pairwise as P1 to P6, P2 to P5, and P3 to P4, via branches of localized patterns without snaking. Finally, from the 7th and last unaccounted simple bifurcation point on S7 there bifurcates a branch which connects to the S8.5 branch. Thus, even on the small domain we have some rather complicated secondary bifurcations from the stripes, but of all the branches discussed above only S7 and the snakes connecting to S7 have some stable parts for $\lambda > 3$.

Remark 3.4. Looking at the stability indices, i.e., the number of positive eigenvalues and the eigenvalues themselves, on the branches we also find a Hopf point near the fold of S7, see Fig. 16(a). This, however, will be studied elsewhere.]

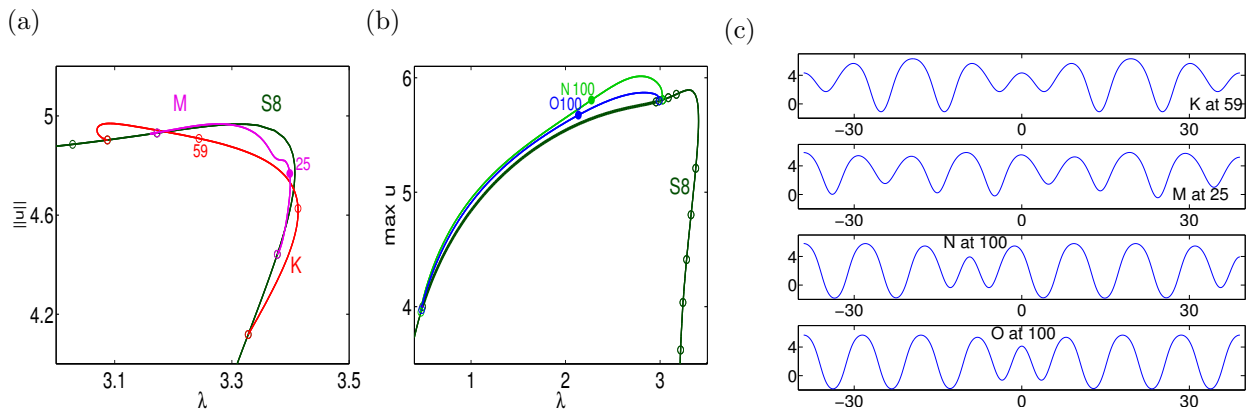


Figure 17: Bifurcations from the remaining bifurcation points on S8.

4 Outlook: additional numerical results

4.1 Fully localized spot patches over radial stripes

Besides the straight (planar) stripes considered so far, we may expect so called radial stripes which only depend on the radius r and are asymptotically periodic in r , see, e.g., [Sch03]. Moreover, for the 2D quadratic–cubic and cubic–quintic SHe (1) and (2) also a number of localized radial stripe patterns are known, e.g., radial pulses (or spots) and rings [LSAC08, Figure 1 and §5], see also [LS09], and again these patterns can also be expected for RD systems with a Turing instability, cf. [LS09, Remark 1].

Thus we may search for such solutions of (4) or (7), and may study their bifurcations to patterns with (dihedral) D_n symmetry, including some fully localized patterns. Here we restrict to (4), i.e., let $\sigma = 0$ again, over circular sectors with opening angle $\pi/3$, thus effectively restricting to patterns with D_6 symmetry. Again we choose some rather small domain

$$\Omega_r = \{(x, y) = \rho(\cos \phi, \sin \phi) : 0 < \rho < r, 0 < \phi < \pi/3\},$$

with Neumann boundary conditions, and $r = 12\pi/k_c$ (this precise value of r is rather arbitrary, even if we expect radial stripes with asymptotic period $2\pi/k_c$), which yields some interesting results at acceptable numerical costs. (Typically we need meshes of about 60.000 triangles, locally refined near $(x, y) = (0, 0)$, to avoid branch jumping.)

Already the bifurcations from the trivial branch (Fig. 18(a)) show a number of interesting directions, but we focus on the branch **rs** (radial stripes, see Remark 4.1(iii) on that terminology) coming from branch point 6. The bifurcation diagram in (b) shows that similar to the straight stripes from §2 the radial stripes bifurcate supercritically but unstable, gain stability at some $\lambda_{rs}^b \approx 3.15$ and loose stability again at $\lambda = \lambda_{rs}^e \approx 2.82$. The example plots in (c),(d) show that **rs** starts as a “hot stripe” with a peak in 0, and after losing stability turns around to return to the homogeneous branch as a “cold stripe” with a slightly longer period. See also Remark 4.1(iv) on the “cold stripe” half of **rs** branch.

In Fig. 19 we show the bifurcation of spot patches from the radial stripes at λ_{rs}^e . The tangent at bifurcation Fig. 18(c) shows that we may expect one sixth of a regular hexagon patch to appear near 0, and this indeed happens on the **sp** branch. During continuation the branch snakes as additional spots are added, with alternating stable and unstable parts of the branch. Except for the central hexagon, the added spots yield somewhat distorted hexagon patches, and as the spots approach the radial boundary of the domain the numerical continuation becomes difficult: the mirror symmetry along angle $\pi/6$ is lost due to numerical inaccuracy somewhere beyond point 120, the stepsize

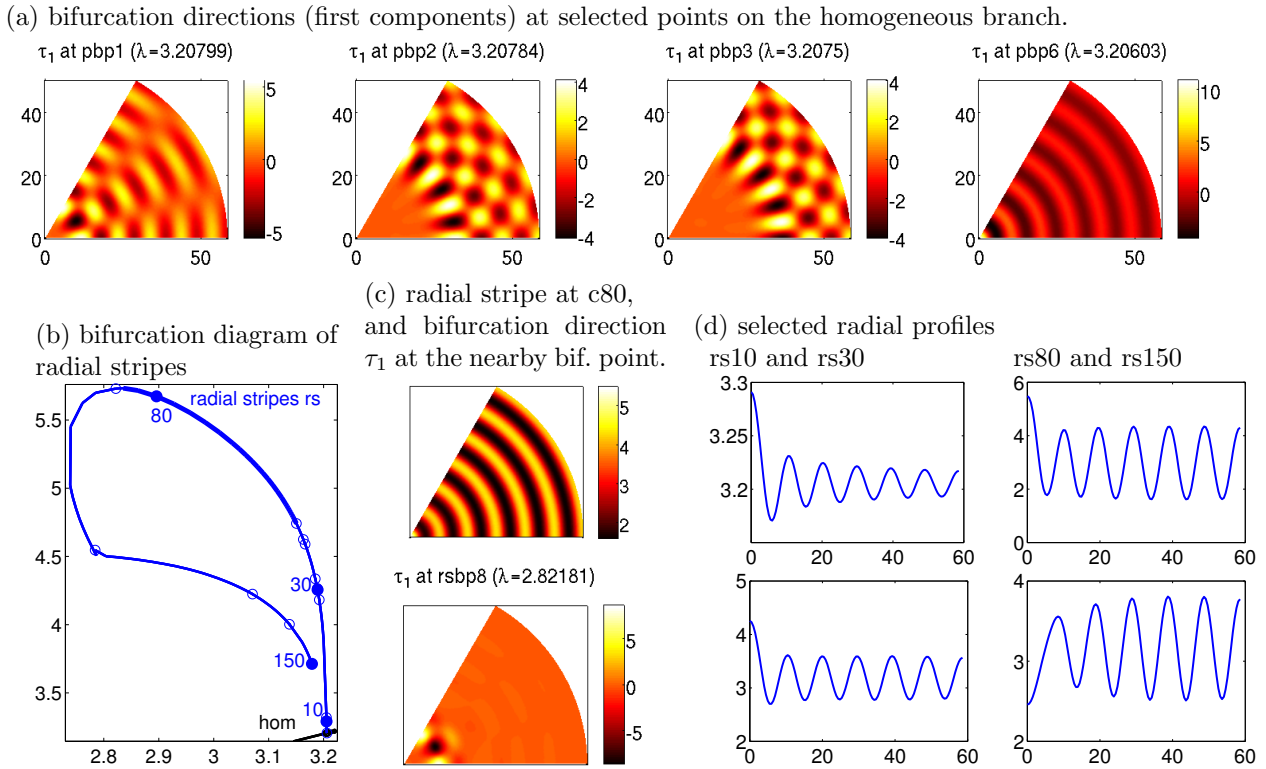


Figure 18: Bifurcation of radial stripes from the homogeneous branch $w(\lambda) = (\lambda, 1/\lambda)$ over a sector with radius $r = 12\pi/k_c$ and angle $\pi/3$. (a) Some bifurcation directions from w . (b)-(d) Bifurcation diagram and some example plots, including the bifurcation direction to the spot patch branch, see Fig. 19.

decreases quickly, and eventually continuation fails. Figure 19(c) shows the five-fold rotation of sp60 , while Fig. 2(d) in the Introduction is obtained from sp40 in the same way.

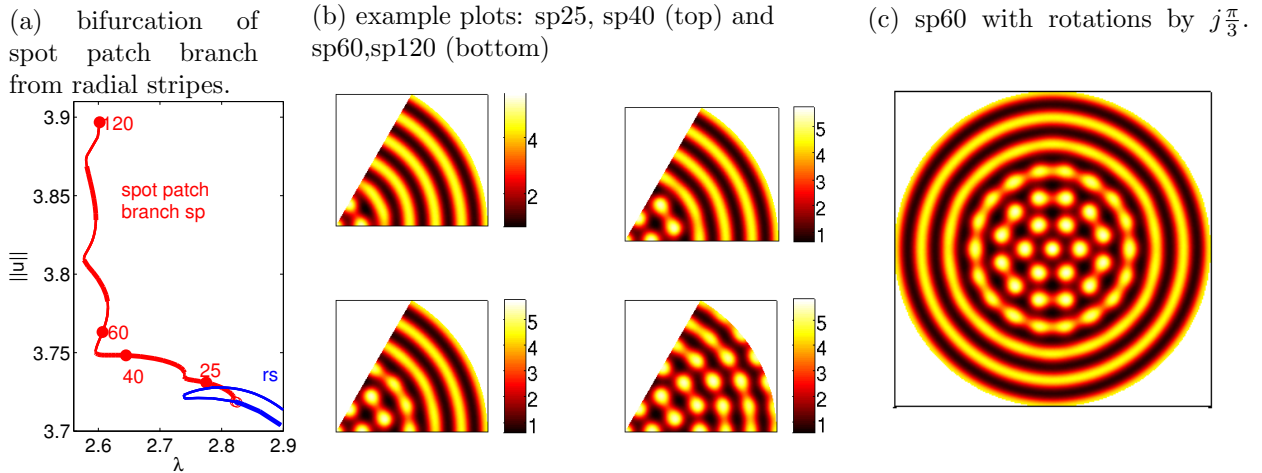


Figure 19: Bifurcation of (hexagonal, in center) spot patch branch sp from radial stripes. See [UW13] for a movie.

As this section is only intended as an outlook, and as we plan to study at least some of these patterns elsewhere, including some analytical approaches in the spirit of [LS09], here we close with the following remarks.

Remark 4.1. (i) Branch switching at some other bifurcation points on the homogeneous branch gives a number of interesting different patterns, see Fig. 18(a) for some example bifurcation

directions. However, in contrast to the radial stripes, all of these appear to depend strongly on the somewhat artificial choice of the bounded domain, in particular the radial Neumann boundary conditions.

- (ii) Some of the earlier bifurcation points on the **rs** branch do give localized patterns, where, e.g., one of the “middle” stripes is replaced by a spot ring, but these are unstable.
- (iii) From the bifurcation direction in Fig. 18(a), and from the radial profiles near bifurcation, e.g., **rs10** in (d), it appears that the **rs** branch should rather be classified as a radial spot branch, i.e., solutions show radially decaying oscillations. However, since the branch continuously turns into non-decaying oscillations we find the name radial stripes more appropriate. Presumably, one needs significantly larger domains to cleanly distinguish radial spots and stripes. The same applies to radial rings, which following [LS09, Theorem 1, Remark 1] we may expect for (7) with $\sigma < \sigma_c$ where we have a subcritical bifurcation of (straight) stripes.
- (iv) From the “cold” branch bifurcating from the homogeneous branch at the same point as the “hot” **rs** branch but in the opposite direction we obtain a bifurcation of a “cold” spot branch.
- (v) It appears natural to conjecture that also localized radial stripes (i.e., spots or rings) over a background of hexagons should exist. To find these we considered triangular domains as in Fig. 11, which support hexagon patterns, and looked for radial stripes near $(x, y) = 0$ by two methods: (a) via bifurcation as the hot hexagons gain stability roughly at λ_{hh}^b (the start of the bean branch over rectangular domains); (b) by using suitable initial guesses and time integration or a direct Newton loop. Both methods failed so far.

]

4.2 An interface perpendicular to stripes

For all planar fronts so far we chose different lengths in x but kept the y dimension fixed and rather small. Together with the choice of vertical stripes this gave interfaces parallel to the stripes, and essentially this also holds true for the interfaces to radial stripes in §4.1. We now aim at more general interfaces, and thus first consider *long* vertical stripes, i.e., large y -lengths. Figure 20 shows some branches of solutions and example plots over the 1×6 domain $\Omega = (-\frac{2\pi}{k_c}, \frac{2\pi}{k_c}) \times (-\frac{12\pi}{\sqrt{3}k_c}, \frac{12\pi}{\sqrt{3}k_c})$. Decreasing λ , the stripes no longer lose stability at $\lambda_s^e \approx 2.51$ to the regular beans with $k_{2,3} = \frac{k_c}{2}(-1, \sqrt{3})$, but earlier to stretched beans with wave vectors $k_{2,3} = \frac{k_c}{7}(-\frac{1}{2}, \pm\frac{13}{12}\frac{\sqrt{3}}{2})$, denoted by **b1**, with 6.5 spots in y -direction. This branch *turns* into a stretched hexagon branch, becoming stable in a fold. The regular beans **b3** bifurcate at the third bifurcation point after loss of stability of the stripes and contain a number of bifurcation points. Two of the bifurcation points on **b3** are connected by a front in x -direction. However, on the example branch **11** the solutions first change wave-number near the top and the bottom and then become very similar to hexagons with 7 spots in y -direction, and similar effects occur on branches from the remaining bifurcation points on **b3**.

The **b1** branch contains two bifurcation points which are connected by a branch containing a rather flat vertical front between stripes and (stretched) hexagons, i.e., the interface is perpendicular to the stripes. We did not find similar branches bifurcating from other bean branches, in particular not from the regular beans **b3**. We do not know, why this is so.

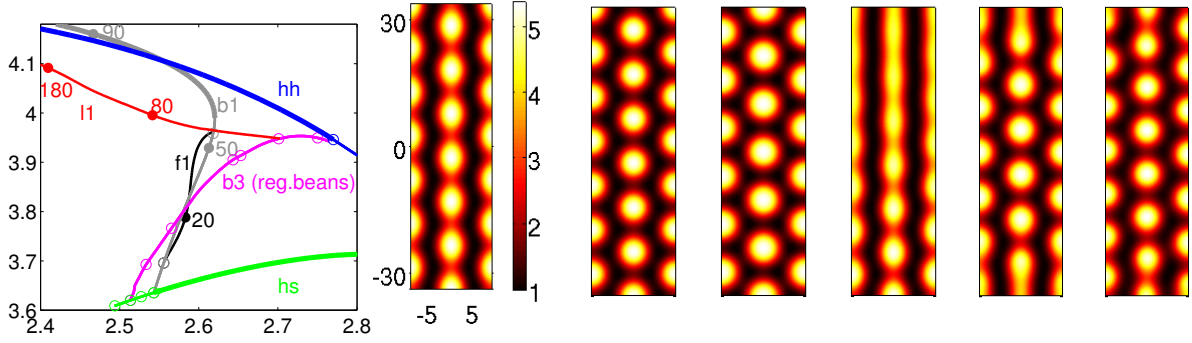
The numerics are considerably more difficult on the 1×6 domain compared to, e.g., the 4×2 from Fig. 5. For instance, in Fig. 20 we had to refine the mesh to about 100000 points on the bifurcating branches to avoid some behaviour like increasingly tilted interfaces during continuation, which do not seem to be due to properties of the PDE, but due to finite size and discretization effects, i.e., poor meshes.

4.3 Fully localized (sideband) hexagon patches over straight stripes

In our final simulation we return to the modified system (21), with $\sigma = -0.3$, mainly because the numerics for fully localized hexagons over stripes appear to be easier in that regime, than, e.g., in

(a) bifurcation diagram

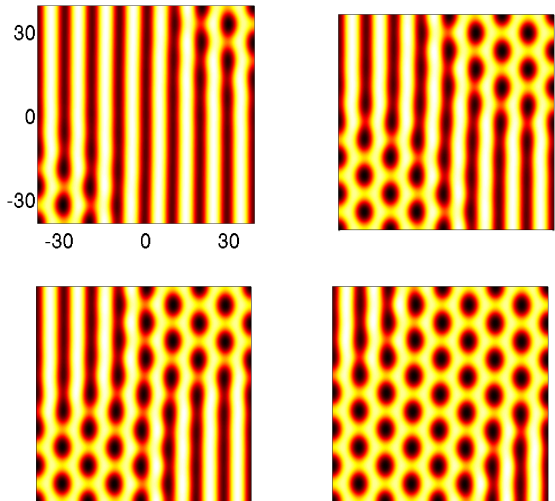
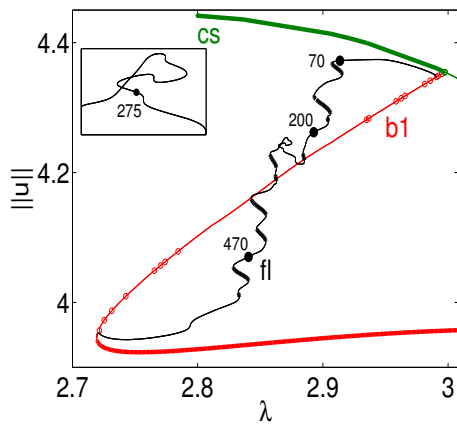
(b) b1-50, b1-90, hh-10, fl-20, l1-80, and l1-180

Figure 20: Bifurcations from the stripes in the hot regime ($\sigma = 0$) over the 1×6 domain.

the hot regime from Fig. 20, where y -fronts are quite flat, while x -fronts are rather steep, cf. §2.2. Since over large domains we then again find that the selected wave vectors for patterns are not necessarily k_1, k_2, k_3 in a hexagonal lattice with $|k_j| = k_c$, here we choose the large square domain $\Omega = (-8\pi/k_c, 8\pi/k_c) \times (-8\pi/k_c, 8\pi/k_c)$. Note the missing $1/\sqrt{3}$ in the y -length, such that this does not allow regular hexagons with wave-vectors $k_{2,3} = k_c(-\frac{1}{2}, \pm\frac{\sqrt{3}}{2})$. Instead, similar to §2.5 and Fig. 20 we expect sideband hexagons with $k_{2,3}$ near $k_c(-\frac{1}{2}, \pm\frac{\sqrt{3}}{2})$, and the closest wave vectors allowed by the domain are $k_{2,3} = k_c(-\frac{1}{2}, \pm\frac{3}{4})$.

(b) fl70, fl200 (top), and fl275, fl470 (bottom)

(a) bifurcation diagram

Figure 21: Fully localized patches of stretched hexagons on a stripe background for $\sigma = -0.3$ over the square domain $\Omega = (-8\pi/k_c, 8\pi/k_c) \times (-8\pi/k_c, 8\pi/k_c)$. Colormap in all plots roughly between 0 and 5. See [UW13] for a movie.

We start at $\lambda = 2.8$ in the stable part of the vertical cold stripes cs for $\sigma = -0.3$ and follow the branch in positive λ direction. When the stripes lose their stability, there bifurcates a bean-branch $b1$, which *turns* into a branch of (stretched) cold hexagons and connects to the homogeneous branch at λ very close to λ_c . As expected, the patterns of $b1$ are stretched in vertical direction, i.e., $k_{2,3} = k_c(-1/2, \pm 3/4)$. From the first bifurcation point on $b1$ bifurcates a (snaking) branch of horizontal planar fronts between the $b1$ hexagons and the stripes cs , i.e., similar to Fig. 10, or rather similar to Fig. 15(f), while from the second bifurcation point bifurcates a (snaking) branch of planar fronts perpendicular to the stripe direction, similar to $f1$ in Fig. 20.

Finally, from the third bifurcation point on **b1** a branch **f1** of fully localized hexagon patches bifurcates. At the beginning the solutions have a patch of (stretched) hexagons in two corners, see **f1p70** of Fig. 21(c). The branch snakes and the patches grow towards the middle (**f1p200**). At **f1p275** the patches get together and the branch makes a loop, such that afterwards we rather have two patches of stripes on a hexagon background, see, e.g., **f1p400**.

Clearly, as for §4.1, many open questions remain for the patterns calculated in Fig. 20 and 21.

5 Discussion, and Open Problems

As for localized patterns over homogeneous backgrounds, the main ingredients for localized patterns over a different background pattern is a bistable range, usually generated by a subcritical bifurcation (of mixed modes, in the case of two patterns). For planar interfaces the existence and approximate location of the pinning region can be predicted if there exists a heteroclinic connection between the corresponding fixed points in the associated Ginzburg–Landau system at some Maxwell point $\lambda = \lambda_m$. The pinning effect in the full system then yields the existence of heteroclinics in a parameter interval around λ_m , and the same effect yields branches of localized patterns in a patterned background even if the Ginzburg–Landau system only has “approximate” homoclinic solutions.

These results have already been suggested in [Pom86], and have been further worked out in 1D problems and for patterns over homogeneous background in various papers cited above, but §2 of the present paper appears to be the first numerical illustration for different patterns in 2D. Moreover, in §4 we gave a numerical outlook on some classes of fully localized patterns over patterns. All the numerics are somewhat delicate due to the very many solution branches that exist in the Turing unstable range, in particular over large domains, which require rather fine discretizations to avoid uncontrolled branch switching. Here we restricted to domains of still small to intermediate size.

The results are certainly not special for the model problems (4), (7), and we have for instance used the same method to predict and numerically find various snaking branches in other 2D reaction diffusion systems [WF13].

Our work has been almost entirely numerical, and at many places we just give first steps towards understanding the new patterns found. Main Open Problems and “things to do” include (in order of appearance):

- (a) Clarify why the snaking in the hot regime is strongly slanted, see Fig. 7.
- (b) Derive a formula like (10) giving exponential smallness of the snaking width in the subcriticality parameter ε . For (7) this should probably be done near the codimension 2 point (λ_c, σ_c) , cf. Remark 3.3(a). Alternatively, discuss this near a codimension 2 point for the full Selkov–Schnakenberg model using (at least one of) the parameters a, b discussed after (3).
- (c) Following (b), or independently, calculate more numerical data for the relation of subcriticality and snaking width using fold continuation, cf. Remark 3.3(b).
- (d) Detect and study Hopf bifurcations in (4) or (7), see Remark 3.4 for just one example.
- (e) Study, both numerically and analytically, fully localized patterns over patterns in more detail; in §4 we gave just a very first outlook of these.

Additionally, it might be interesting to study the stick–slip motion (Fig. 9) near a snake in more detail, including the derivation of equations of motion for interfaces. For (c) and (d), here we refrain from setting up ad hoc modifications of `pde2path`, but instead plan to include the needed upgrades (multi–parameter continuation and Hopf bifurcation) in a general way into the package.

References

- [ALB⁺10] D. Avitabile, D.J.B. Lloyd, J. Burke, E. Knobloch, and B. Sandstede. To snake or not to snake in the planar Swift–Hohenberg equation. *SIAM J. Appl. Dyn. Syst.*, 9(3):704–733, 2010.

- [BBKM08] A. Bergeom, J. Burke, E. Knobloch, and I. Mercader. Eckhaus instability and homoclinic snaking. *Phys.Rev.E*, 78:025201, 2008.
- [BCR08] U. Bortolozzo, M. G. Clerc, and S. Residori. Local theory of the slanted homoclinic snaking bifurcation diagram. *Phys. Rev. E*, 78:036214, Sep 2008.
- [BD12] J. Burke and J. Dawes. Localized states in an extended Swift–Hohenberg equation. *SIAM J. Appl. Dyn. Syst.*, 11(1):261–284, 2012.
- [BK06] J. Burke and E. Knobloch. Localized states in the generalized Swift-Hohenberg equation. *Phys. Rev. E*, 73:056211, May 2006.
- [BK07] J. Burke and E. Knobloch. Homoclinic snaking: Structure and stability. *Chaos*, 17(3):037102, 15 p., 2007.
- [BKL⁺09] M. Beck, J. Knobloch, D.J.B. Lloyd, B. Sandstede, and T. Wagenknecht. Snakes, ladders, and isolas of localized patterns. *SIAM J. Math. Anal.*, 41(3):936–972, 2009.
- [BvHS95] P. Bollermann, A. van Harten, and G. Schneider. On the justification of the Ginzburg–Landau approximation. In A. Doelman and A. van Harten, editors, *Nonlinear dynamics and pattern formation in the natural environment*, pages 20–37. Longman UK, 1995.
- [CH93] M.C. Cross and P.C. Hohenberg. Pattern formation outside equilibrium. *Rev. Mod. Phys.*, 65:854–1190, 1993.
- [CK09] S.J. Chapman and G. Kozyreff. Exponential asymptotics of localised patterns and snaking bifurcation diagrams. *Physica D*, 238(3):319–354, 2009.
- [CP90] J. Carr and R. Pego. Invariant manifolds for metastable patterns in $u_t = \varepsilon^2 u_{xx} - f(u)$. *Proc. R. Soc. Edinb., Sect. A*, 116(1-2):133–160, 1990.
- [Daw09] J. Dawes. Modulated and localized states in a finite domain. *SIAM J. Appl. Dyn. Syst.*, 8(3):909–930, 2009.
- [DMCK11] A.D. Dean, P.C. Matthews, S.M. Cox, and J.R. King. Exponential asymptotics of homoclinic snaking. *Nonlinearity*, 24(12):3323–3351, 2011.
- [DRvdS12] A. Doelman, J. D. M. Rademacher, and S. van der Stelt. Hopf dances near the tips of Busse balloons. *Discrete Contin. Dyn. Syst. Ser. S*, 5(1), 2012.
- [DSSS03] A. Doelman, B. Sandstede, A. Scheel, and G. Schneider. Propagation of hexagonal patterns near onset. *European J. Appl. Math.*, 14(1):85–110, 2003.
- [GSK84] M. Golubitsky, J.W. Swift, and E. Knobloch. Symmetries and Pattern selection in Rayleigh-Benard convection. *Physica*, 10 D:249–276, 1984.
- [HK09] S. M. Houghton and E. Knobloch. Homoclinic snaking in bounded domains. *Phys.Rev.E*, 80:026210, 2009.
- [HMBD95] M. F. Hilali, S. Métens, P. Borckmans, and G. Dewel. Pattern selection in the generalized Swift-Hohenberg model. *Phys. Rev. E*, 51:2046–2052, Mar 1995.
- [Hoy06] R.B. Hoyle. *Pattern formation*. Cambridge University Press., Cambridge, UK, 2006.
- [KAC09] G. Kozyreff, P. Assemat, and S.J. Chapman. Influence of boundaries on localized patterns. *Phys. Rev. Letters*, 103:164501, 2009.
- [KC06] G. Kozyreff and S.J. Chapman. Asymptotics of large bound states of localized structures. *Phys. Rev. Letters*, 97(4):044502, 2006.
- [KC13] G. Kozyreff and S.J. Chapman. Analytical results for Front Pinning between an Hexagonal Pattern and a Uniform State in Pattern-Formation Systems. *Phys. Rev. Letters*, 111(5):054501, 2013.
- [Kno08] E. Knobloch. Spatially localized structures in dissipative systems: open problem. *Nonlinearity*, 21:T45–T60, 2008.
- [LJBK11] D. Lo Jacono, A. Bergeon, and E. Knobloch. Magnetohydrodynamic convectons. *J. Fluid Mech.*, 687:595–605, 2011.

- [LO13] D. Lloyd and H. O’Farrell. On localised hotspots of an urban crime model. *Physica D*, 253:23–39, 2013.
- [LS09] D. Lloyd and B. Sandstede. Localized radial solutions of the Swift-Hohenberg equation. *Non-linearity*, 22(2):485–524, 2009.
- [LSAC08] D.J.B. Lloyd, B. Sandstede, D. Avitabile, and A.R. Champneys. Localized hexagon patterns of the planar Swift-Hohenberg equation. *SIAM J. Appl. Dyn. Syst.*, 7(3):1049–1100, 2008.
- [Mie02] A. Mielke. The Ginzburg-Landau equation in its role as a modulation equation. In *Handbook of dynamical systems, Vol. 2*, pages 759–834. North-Holland, 2002.
- [MNT90] B.A. Malomed, A.A. Nepomnyashchy, and M.I. Tribelsky. Domain boundaries in convection patterns. *Phys.Rev.A*, 42(12):7244–7263, 1990.
- [Mur89] J.D. Murray. *Mathematical biology*. Springer-Verlag, Berlin, 1989.
- [NG06] A.A. Nepomnyashchy and A.A. Golovin. General aspects of pattern formation. In A.A. Nepomnyashchy and A.A. Golovin, editors, *Self-Assembly, Pattern Formation and Growth Phenomena in Nano-Systems*, pages 1–54. Springer, 2006.
- [Pis06] L.M. Pismen. *Patterns and interfaces in dissipative dynamics*. Springer, 2006.
- [Pom86] Y. Pomeau. Front motion, metastability and subcritical bifurcations in hydrodynamics. *Physica D*, 23:3–11, 1986.
- [Sch79] J. Schnakenberg. Simple chemical reaction systems with limit cycle behaviour. *Journal of Theoretical Biology*, 81:389–400, 1979.
- [Sch94] G. Schneider. Error estimates for the Ginzburg–Landau approximation. *ZAMP*, 45:433–457, 1994.
- [Sch99] G. Schneider. Global existence results in pattern forming systems – Applications to 3D Navier–Stokes problems –. *J. Math. Pures Appl.*, IX, 78:265–312, 1999.
- [Sch03] A. Scheel. Radially symmetric patterns of reaction-diffusion systems. *Mem. Am. Math. Soc.*, 786:86, 2003.
- [Sel68] E.E. Sel’kov. Self-oscillations in glycolysis. *European Journal of Biochemistry*, 4(1):79–86, 1968.
- [SM11] H. Susanto and P.C. Matthews. Variational approximations to homoclinic snaking. *Phys. Rev. E*, 83:035201(R), 2011.
- [UW13] H. Uecker and D. Wetzel. www.staff.uni-oldenburg.de/hannes.uecker/pde2path/schnakmov.html, 2013.
- [UWR13] H. Uecker, D. Wetzel, and J. Rademacher. pde2path – a Matlab package for continuation and bifurcation in 2D elliptic systems. Preprint, 50p, to appear in *Numerical Mathematics: Theory, Methods, Application*. www.staff.uni-oldenburg.de/hannes.uecker/pde2path/index.html, 2013.
- [WF13] D. Wetzel and U. Feudel. Snaking between Turing patterns in some benthic predator prey models. In Preparation, 2013.
- [Yan04] L Yang. Stable squares and other oscillatory Turing patterns in a reaction-diffusion model. *Phys. Rev. Letters*, 92(19):198303–1, 2004.